Solutions of the Euler and the Laminar and Turbulent Navier-Stokes Equations in Two-Dimensions Using TVD and ENO Algorithms

EDISSON SÁVIO DE GÓES MACIEL
IEA- Aeronautical Engineering Division
ITA – Aeronautical Technological Institute
Praça Mal. Eduardo Gomes, 50 – Vila das Acácias – São José dos Campos – SP – 12228-900
BRAZIL
edissonsavio@yahoo.com.br

Abstract: - In the present work, the Yee, Warming and Harten and the Yang schemes are implemented, on a finite volume context and using a structured spatial discretization, to solve the Euler and the Navier-Stokes equations in two-dimensions. The former is a TVD high resolution scheme, whereas the latter is an ENO/TVD high resolution algorithm. Both schemes are flux difference splitting ones. An implicit formulation is employed to solve the Euler equations, whereas the Navier-Stokes equations are solved by an explicit formulation. Turbulence is taken into account considering the models of Cebeci and Smith, of Baldwin and Lomax and of Sparlat and Allmaras. The physical problems of the transonic flow along a convergent-divergent nozzle and the supersonic flow along a compression corner are studied in the inviscid case. In the viscous case, the supersonic flow along a ramp is solved. The results have demonstrated that all three algorithms present accurate results.

Key-Words: - Yee, Warming and Harten algorithm, TVD high resolution scheme, Yang algorithms, ENO/TVD high resolution schemes, Euler and Navier-Stokes equations, Turbulence models.

1 Introduction

Conventional shock capturing schemes for the solution of nonlinear hyperbolic conservation laws are linear and L_2-stable (stable in the L_2-norm) when considered in the constant coefficient case ([1]). There are three major difficulties in using such schemes to compute discontinuous solutions of a nonlinear system, such as the compressible Euler equations:

(i) Schemes that are second (or higher) order accurate may produce oscillations wherever the solution is not smooth;

(ii) Nonlinear instabilities may develop in spite of the L_2-stability in the constant coefficient case;

(iii) The scheme may select a nonphysical solution.

It is well known that monotone conservative difference schemes always converge and that their limit is the physical weak solution satisfying an entropy inequality. Thus monotone schemes are guaranteed not to have difficulties (ii) and (iii). However, monotone schemes are only first order accurate. Consequently, they produce rather crude approximations whenever the solution varies strongly in space or time.

When using a second (or higher) order accurate scheme, some of these difficulties can be overcome by adding a hefty amount of numerical dissipation to the scheme. Unfortunately, this process brings about an irretrievable loss of information that exhibits itself in degraded accuracy and smeared discontinuities. Thus, a typical complaint about conventional schemes which are developed under the guidelines of linear theory is that they are not robust and/or not accurate enough.

To overcome the difficulties, a new class of schemes was considered that is more appropriate for the computation of weak solutions (i.e., solutions with shocks and contact discontinuities) of nonlinear hyperbolic conservation laws. These schemes are required (a) to be total variation diminishing in the nonlinear scalar case and the constant coefficient system case ([2-3]) and (b) to be consistent with the conservation law and an entropy inequality ([4-5]). The first property guarantees that the scheme does not generate spurious oscillations. Schemes with this property are referred in the literature as total variation diminishing (TVD) schemes (or total variation non-increasing, TVNI, [3]). The latter property guarantees that the weak solutions are physical ones. Schemes in this class are guaranteed to avoid difficulties (i)-(iii) mentioned above.

[6] applied a new implicit unconditionally stable high resolution TVD scheme to steady state calculations. It was a member of a one-parameter family of explicit and implicit second order accurate schemes developed by [3] for the computation of weak solutions of one-dimensional hyperbolic conservation laws. The scheme was guaranteed not to generate spurious oscillations for a nonlinear scalar equation and a constant coefficient system.

Numerical experiments have shown that the scheme not only had a fairly rapid convergence rate, but also generated a highly resolved approximation to the steady state solution. A detailed implementation of the implicit scheme for the one- and two-dimensional compressible inviscid equations of gas dynamics was presented. Some numerical experiments of one- and two-dimensional fluid flows containing shocks demonstrated the efficiency and accuracy of the new scheme.

Recently, a new class of uniformly high order accurate essentially nonoscillatory (ENO) schemes have been developed by [7-10]. They presented a hierarchy of uniformly high order accurate schemes that generalize [11]'s scheme, its second order accurate MUSCL extension ([12-13]), and the total variation diminishing (TVD) scheme ([3]) to arbitrary order of accuracy. In contrast to the earlier second order TVD schemes which drop to first order accuracy at local extrema and maintain second order accuracy in smooth regions, the new ENO schemes are uniformly high order accurate throughout, even at critical points. The ENO schemes use a reconstruction algorithm that is derived from a new interpolation technique that when applied to piecewise smooth data gives high order accuracy whenever the function is smooth but avoids a Gibbs phenomenon at discontinuities. An adaptive stencil of grid points is used; therefore, the resulting schemes are highly nonlinear even in the scalar case.

[14] has presented a two time level explicit and implicit finite difference shock capturing schemes based on the characteristic flux difference splitting method and the modified flux approach with the essentially nonoscillatory (ENO) property that [7] have been developed for the two-dimensional Euler equations. The methods were conservative, uniformly second order accurate in time and space, even at local extrema. General coordinate systems were used to treat complex geometries. Standard alternating direction implicit approximate factorization was used for constructing implicit schemes. Numerical results have been obtained for unsteady shock wave reflection around general two-dimensional blunt body and for steady transonic flows over a circular arc bump in a channel. Properties of ENO schemes as applied to two-dimensional flows with multiple embedded discontinuities were discussed. Comparisons of the performance between the presented ENO schemes and author's previous total variation diminishing schemes were also included. The [14] scheme could be ENO or TVD ones depending of the choice of a free parameter.

There is a practical necessity in the aeronautical industry and in other fields of the capability of calculating separated turbulent compressible flows. With the available numerical methods, researches seem able to analyze several separated flows, three-dimensional in general, if an appropriated turbulence model is employed. Simple methods as the algebraic turbulence models of [15-16] supply satisfactory results with low computational cost and allow that the main features of the turbulent flow be detected.

More elaborate treatments of turbulent flow, especially involving separation, are obtained with one-equation turbulence models. Such models are cheaper than their counterpart two-equation models and a bit more expensive than the algebraic models. One such a model is the [17] one. In this model, a transport equation for the turbulent viscosity is assembled, using empiricism and arguments of dimensional analysis, Galilean invariance and selective dependence on the molecular viscosity. The equation includes a destruction term that depends on the distance to the wall, related to the one in [18] model and to one due to [19]. Unlike early one-equation models, the resulting turbulence model is local (i.e., the equation at one point does not depend on the solution at others points) and therefore compatible with grids of any structure and Navier-Stokes solvers in two- and three-dimensions. It is numerically forgiving, in terms of near-wall resolution and stiffness, and yields rapid convergence to steady state.

In the present work, the [6] and the [14] schemes are implemented, on a finite volume context and using a structured spatial discretization, to solve the Euler and the laminar/turbulent Navier-Stokes equations in the two-dimensional space. The [6] scheme and the [14] schemes are TVD or ENO high resolution flux difference splitting ones, based on the concept of Harten's modified flux function. The [6] TVD scheme is second order accurate in space, except at extrema, where the accuracy is reduced to first order. The [14] scheme, in its ENO version, is uniformly second order accurate in space, inclusive at extrema. Its TVD version is also second order accurate in space, except at extrema. An implicit formulation is employed to solve the Euler equations in the inviscid problems. An approximate factorization ADI method is employed by both schemes to perform time integration. To solve the laminar/turbulent Navier-Stokes equations, an explicit formulation based on a dimensional splitting procedure is employed. All schemes are first order accurate in time in their implicit and explicit versions. Turbulence is taken into account

considering two algebraic models, namely: the [15-16] ones, and the one-equation model of [17]. The algorithms are accelerated to the steady state solution using a spatially variable time step, which has demonstrated effective gains in terms of convergence rate ([20-21]). Two versions of time step definition, which consider inviscid and viscous cases separately, are employed. All schemes are applied to the solution of the physical problems of the transonic flow along a convergent-divergent nozzle and the supersonic flow along a compression corner in the inviscid case (Euler equations). To the laminar/turbulent viscous case, the supersonic flow along a ramp is solved. The results have demonstrated that the most severe results are obtained with the [6] TVD high resolution scheme in the inviscid problems, whereas the [14]/ENO high resolution algorithm present the most severe results in the viscous problem, in both laminar and turbulent cases. The most accurate results are obtained by the [6] TVD scheme in the nozzle problem, by the [14]/ENO scheme in the compression corner problem, both inviscid cases, and by the [14]/TVD scheme in the ramp problem, viscous case.

2 Navier-Stokes Equations

As the Euler equations can be obtained from the Navier-Stokes ones by disregarding the viscous vectors, only the formulation to the latter will be presented. The Navier-Stokes equations in integral conservative form, employing a finite volume formulation and using a structured spatial discretization, to two-dimensional simulations, are written as:

$$\partial Q/\partial t + 1/V \int_V \vec{\nabla} \cdot \vec{P} dV = 0 , \qquad (1)$$

where V is the cell volume, which corresponds to an rectangular cell in the two-dimensional space; Q is the vector of conserved variables; and $\vec{P} = (E_e - E_v)\vec{i} + (F_e - F_v)\vec{j}$ represents the complete flux vector in Cartesian coordinates, with the subscript "e" related to the inviscid contributions or the Euler contributions and "v" is related to the viscous contributions. These components of the complete flux vector, as well the vector of conserved variables, are defined as:

$$Q = \begin{Bmatrix} \rho \\ \rho u \\ \rho v \\ e \end{Bmatrix}, \; E_e = \begin{Bmatrix} \rho u \\ \rho u^2 + p \\ \rho uv \\ (e+p)u \end{Bmatrix}, \; F_e = \begin{Bmatrix} \rho v \\ \rho uv \\ \rho v^2 + p \\ (e+p)v \end{Bmatrix}; \qquad (2)$$

$$E_v = \frac{1}{\mathrm{Re}} \begin{Bmatrix} 0 \\ \tau_{xx} \\ \tau_{xy} \\ \tau_{xx}u + \tau_{xy}v - q_x \end{Bmatrix}, \; F_v = \frac{1}{\mathrm{Re}} \begin{Bmatrix} 0 \\ \tau_{yx} \\ \tau_{yy} \\ \tau_{yx}u + \tau_{yy}v - q_y \end{Bmatrix}. \qquad (3)$$

In these equations, the components of the viscous stress tensor are defined as:

$$\tau_{xx} = 2(\mu_M + \mu_T)\partial u/\partial x - 2/3(\mu_M + \mu_T)(\partial u/\partial x + \partial v/\partial y); \quad (4)$$

$$\tau_{xy} = (\mu_M + \mu_T)(\partial u/\partial y + \partial v/\partial x) ; \qquad (5)$$

$$\tau_{yy} = 2(\mu_M + \mu_T)\partial v/\partial y - 2/3(\mu_M + \mu_T)(\partial u/\partial x + \partial v/\partial y). \quad (6)$$

The components of the conductive heat flux vector are defined as follows:

$$q_x = -\gamma(\mu_M/\mathrm{Pr}d + \mu_T/\mathrm{Pr}d_T)\partial e_i/\partial x ; \qquad (7)$$

$$q_y = -\gamma(\mu_M/\mathrm{Pr}d + \mu_T/\mathrm{Pr}d_T)\partial e_i/\partial y . \qquad (8)$$

The quantities that appear above are described as follows: ρ is the fluid density, u and v are the Cartesian components of the flow velocity vector in the x and y directions, respectively; e is the total energy per unity volume of the fluid; p is the fluid static pressure; e_i is the fluid internal energy, defined as:

$$e_i = e/\rho - 0.5(u^2 + v^2); \qquad (9)$$

the τ's represent the components of the viscous stress tensor; Prd is the laminar Prandtl number, which assumed a value of 0.72 in the present simulations; Prd_T is the turbulent Prandtl number, which assumed a value of 0.9; the q's represent the components of the conductive heat flux; μ_M is the fluid molecular viscosity; μ_T is the fluid turbulent viscosity; γ is the ratio of specific heats at constant pressure and volume, respectively, which assumed a value 1.4 to the atmospheric air; and Re is the Reynolds number of the viscous simulation, defined by:

$$\mathrm{Re} = \rho u_{REF} l/\mu_M , \qquad (10)$$

where u_{REF} is a characteristic flow velocity and l is a configuration characteristic length. The molecular viscosity is estimated by the empiric Sutherland formula:

$$\mu_M = bT^{1/2}/(1 + S/T), \qquad (11)$$

where T is the absolute temperature (K), b = 1,458x10^{-6} Kg/(m.s.K$^{1/2}$) and S = 110,4 K, to the atmospheric air in the standard atmospheric conditions ([22]). The Navier-Stokes equations were nondimensionalized in relation to the stagnation density, ρ_*, and the critical speed of sound, a_*, for the nozzle problem, whereas in relation to the freestream density, ρ_∞, and the freestream speed of sound, a_∞, for the compression corner problem. For the ramp problem it is also considered the freestream molecular viscosity, μ_∞. To allow the solution of the matrix system of four equations to four unknowns described by Eq. (1), it is employed the state equation of perfect gases presented below:

$$p = (\gamma - 1)\left[e - 0.5\rho(u^2 + v^2)\right]. \quad (12)$$

The total enthalpy is determined by:

$$H = (e + p)/\rho\,. \quad (13)$$

3 Numerical Scheme of [6]

The [6] algorithm, second order accurate in space, is specified by the determination of the numerical flux vector at (i+½,j) interface. The implementation of the other numerical flux vectors at the other interfaces is straightforward.

Following a finite volume formalism, which is equivalent to a generalized system, the right and left cell volumes, as well the interface volume, necessaries to coordinate change, are defined by:

$$V_R = V_{i+1,j},\ V_L = V_{i,j} \ \text{ and } \ V_{\text{int}} = 0.5(V_R + V_L)\,. \quad (14)$$

where "R" and "L" represent right and left, respectively. The cell volume is defined by:

$$V_{i,j} = 0.5\left|\left(x_{i,j} - x_{i+1,j}\right)y_{i+1,j+1} + \left(x_{i+1,j} - x_{i+1,j+1}\right)y_{i,j} + \left(x_{i+1,j+1} - x_{i,j}\right)y_{i+1,j}\right| +$$

$$0.5\left|\left(x_{i,j} - x_{i+1,j+1}\right)y_{i,j+1} + \left(x_{i+1,j+1} - x_{i,j+1}\right)y_{i,j} + \left(x_{i,j+1} - x_{i,j}\right)y_{i+1,j+1}\right|, \quad (15)$$

where a computational cell, with its nodes and flux surfaces are defined in [23] and in section 8 of the present work. The area components at interface are defined by: $S_{x\_\text{int}} = s_x^{'}S$ and $S_{y\_\text{int}} = s_y^{'}S$, where $s_x^{'}$ and $s_y^{'}$ are defined as: $s_x^{'} = s_x/S$ and $s_y^{'} = s_y/S$, being $S = \sqrt{s_x^2 + s_y^2}$. Expressions to s_x and s_y, which represent the S_x and S_y components always adopted in the positive orientation, are given in Tab. 1. These normalized area vectors are employed in the [6] TVD high resolution scheme. In the [14] schemes, the area vectors are defined as presented in Tab. 2.

Table 1. Normalized values of s_x and s_y.

Surface	s_x	s_y
i,j-1/2	$-\left(y_{i+1,j} - y_{i,j}\right)$	$\left(x_{i+1,j} - x_{i,j}\right)$
i+1/2,j	$\left(y_{i+1,j+1} - y_{i+1,j}\right)$	$\left(x_{i+1,j} - x_{i+1,j+1}\right)$
i,j+1/2	$\left(y_{i,j+1} - y_{i+1,j+1}\right)$	$\left(x_{i+1,j+1} - x_{i,j+1}\right)$
i-1/2,j	$\left(y_{i,j+1} - y_{i,j}\right)$	$-\left(x_{i,j+1} - x_{i,j}\right)$

Table 2. Values of S_{x_int} and S_{y_int}.

Surface	S_{x_int}	S_{y_int}
i,j-1/2	$\left(y_{i+1,j} - y_{i,j}\right)$	$-\left(x_{i+1,j} - x_{i,j}\right)$
i+1/2,j	$\left(y_{i+1,j+1} - y_{i+1,j}\right)$	$-\left(x_{i+1,j+1} - x_{i+1,j}\right)$
i,j+1/2	$\left(y_{i,j+1} - y_{i+1,j+1}\right)$	$-\left(x_{i,j+1} - x_{i+1,j+1}\right)$
i-1/2,j	$\left(y_{i,j} - y_{i,j+1}\right)$	$-\left(x_{i,j} - x_{i,j+1}\right)$

The metric terms to this generalized coordinate system are defined as:

$$h_x = S_{x\_\text{int}}/V_{\text{int}}\,,\ h_y = S_{y\_\text{int}}/V_{\text{int}} \ \text{ and } \ h_n = S/V_{\text{int}}\,. \quad (16)$$

The properties calculated at the flux interface are obtained either by arithmetical average or by [24] average. In this work, the [24] average was used:

$$\rho_{\text{int}} = \sqrt{\rho_L \rho_R}\,,\ u_{\text{int}} = \left(u_L + u_R\sqrt{\rho_R/\rho_L}\right)/\left(1 + \sqrt{\rho_R/\rho_L}\right); \quad (17)$$

$$v_{\text{int}} = \left(v_L + v_R\sqrt{\rho_R/\rho_L}\right)/\left(1 + \sqrt{\rho_R/\rho_L}\right); \quad (18)$$

$$H_{\text{int}} = \left(H_L + H_R\sqrt{\rho_R/\rho_L}\right)/\left(1 + \sqrt{\rho_R/\rho_L}\right); \quad (19)$$

$$a_{\text{int}} = \sqrt{(\gamma - 1)\left[H_{\text{int}} - 0.5\left(u_{\text{int}}^2 + v_{\text{int}}^2\right)\right]}, \quad (20)$$

where a_{int} is the sound speed at the flux interface. The eigenvalues of the Euler equations, in ξ direction, are given by:

$$U_{cont} = u_{\text{int}}h_x + v_{\text{int}}h_y\,,\ \lambda_1 = U_{cont} - a_{\text{int}}h_n\,; \quad (21)$$

$$\lambda_2 = \lambda_3 = U_{cont} \ \text{ and } \ \lambda_4 = U_{cont} + a_{\text{int}}h_n\,. \quad (22)$$

The jumps of the conserved variables are given by:

$$\Delta\rho = V_{\text{int}}(\rho_R - \rho_L)\,,\ \Delta(\rho u) = V_{\text{int}}\left[(\rho u)_R - (\rho u)_L\right]; \quad (23)$$

$$\Delta(\rho v) = V_{\text{int}}\left[(\rho v)_R - (\rho v)_L\right],\ \Delta e = V_{\text{int}}\left(e_R - e_L\right). \quad (24)$$

The α vectors to the (i+½,j) interface are calculated by the following expressions:

$$\alpha_1 = 0.5(aa - bb),\ \alpha_2 = \Delta\rho - aa,\ \alpha_3 = cc; \quad (25)$$

$$\alpha_4 = 0.5(aa + bb), \quad (26)$$

with:

$$aa = (\gamma - 1)/a_{\text{int}}^2\left[\Delta e + 0.5\left(u_{\text{int}}^2 + v_{\text{int}}^2\right)\Delta\rho - u_{\text{int}}\Delta(\rho u) - v_{\text{int}}\Delta(\rho v)\right]; \quad (27)$$

$$bb = 1/a_{\text{int}}\left[h_x^{'}\Delta(\rho u) - \left(h_x^{'}u_{\text{int}} + h_y^{'}v_{\text{int}}\right)\Delta\rho + h_y^{'}\Delta(\rho v)\right]; \quad (28)$$

$$cc = h_x^{'}\Delta(\rho v) + \left(h_y^{'}u_{\text{int}} - h_x^{'}v_{\text{int}}\right)\Delta\rho - h_y^{'}\Delta(\rho u); \quad (29)$$

$$h_x^{'} = h_x/h_n \quad \text{and} \quad h_y^{'} = h_y/h_n\ . \quad (30)$$

The [6] TVD dissipation function is constructed using the right eigenvector matrix of the Jacobian matrix in the normal direction to the flux face. This matrix is found in [25].

The *g* numerical flux function, which is a limited function to avoid the formation of new extrema in the solution and is responsible to the second order accuracy of the scheme, is given by:

$$g_{i,j}^{1} = \text{signal}_1 \times \text{MAX}\Big[0.0; \left(\sigma_{i+1/2,j}^{1}\left|\alpha_{i+1/2,j}^{1}\right|,\ \text{signal}_1 \times \sigma_{i-1/2,j}^{1}\alpha_{i-1/2,j}^{1}\right)\Big], \quad (31)$$

where $signal_l$ is equal to 1.0 if $\alpha_{i+1/2,j}^{l} \geq 0.0$ and -1.0 otherwise; $\sigma^{l}(\lambda_l) = 0.5Q_l(\lambda_l)$; and Q is defined as:

$$Q_l(Z_l) = \begin{cases} |Z_l|, & if\ |Z_l| \geq \delta_f \\ 0.5\left(Z_l^2 + \delta_f^2\right)/\delta_f, & if\ |Z_l| < \delta_f \end{cases}, \quad (32)$$

where "*l*" varies from 1 to 4 (two-dimensional space) and δ_f assumes values between 0.1 and 0.5, being 0.2 the value recommended by [6]. The θ term, responsible to the artificial compression, which enhances the resolution of the scheme at discontinuities like shock waves and contact discontinuities, is defined as:

$$\theta_{i,j}^{l} = \begin{cases} \left|\alpha_{i+1/2,j}^{l} - \alpha_{i-1/2,j}^{l}\right| \Big/ \left(\left|\alpha_{i+1/2,j}^{l}\right| + \left|\alpha_{i-1/2,j}^{l}\right|\right), & \text{if } \left|\alpha_{i+1/2,j}^{l}\right| + \left|\alpha_{i-1/2,j}^{l}\right| \neq 0.0; \\ 0.0, & \text{if } \left|\alpha_{i+1/2,j}^{l}\right| + \left|\alpha_{i-1/2,j}^{l}\right| = 0.0. \end{cases}$$

(33)

The β parameter at the (i+½,j) interface, which introduces the artificial compression term, is given by:

$$\beta_l = 1.0 + \omega_l\theta_{i,j}^{l}, \quad (34)$$

in which ω_l assumes the following values: $\omega_1 = 0.25$ (non-linear field), $\omega_2 = \omega_3 = 1.0$ (linear field) and $\omega_4 = 0.25$ (non-linear field). The $\tilde{g}$ function is defined by:

$$\tilde{g}_{i,j}^{l} = \beta_l g_{i,j}^{l}. \quad (35)$$

The numerical characteristic speed, φ_l, at the (i+½,j) interface, which is responsible to transport the numerical information associated to the g numerical flux function, or indirectly through $\tilde{g}$, is defined by:

$$\varphi_l = \begin{cases} \left(\tilde{g}_{i+1,j}^{l} - \tilde{g}_{i,j}^{l}\right)/\alpha^{l}, & if\ \alpha^{l} \neq 0.0; \\ 0.0, & if\ \alpha^{l} = 0.0. \end{cases} \quad (36)$$

Finally, the [6] dissipation function, to second order of spatial accuracy, is constructed by the following matrix-vector product:

$$\{D_{YWH}\}_{i+1/2,j} = [R]_{i+1/2,j}\left\{\left(g_{i,j} + g_{i+1,j}\right) - Q(\lambda + \varphi)\alpha\right\}_{i+1/2,j}. \quad (37)$$

The convective numerical flux vector to the (i+½,j) interface is described by:

$$F_{i+1/2,j}^{(l)} = \left(E_{\text{int}}^{(l)}h_x + F_{\text{int}}^{(l)}h_y\right)V_{\text{int}} + 0.5D_{YWH}^{(l)}, \quad (38)$$

with:

$$E_{\text{int}}^{(l)} = 0.5\left(E_R^{(l)} + E_L^{(l)}\right) \text{ and } F_{\text{int}}^{(l)} = 0.5\left(F_R^{(l)} + F_L^{(l)}\right). \quad (39)$$

The right-hand-side of the [6] TVD scheme, necessaries to the resolution of the implicit version of this algorithm, is determined by:

$$\mathrm{RHS(YWH)}^{n}_{i,j} = -\Delta t_{i,j}/V_{i,j}\left(F^{n}_{i+1/2,j} - F^{n}_{i-1/2,j} + F^{n}_{i,j+1/2} - F^{n}_{i,j-1/2}\right). \quad (40)$$

To the viscous simulations, it is necessary to implement the explicit version. In this case, the time integration is replaced by a dimensional splitting method, first order accurate, which divides the temporal integration in two steps, each one associated with a different spatial direction. Considering the initial step associated with the ξ direction:

$$\Delta Q^{*}_{i,j} = -\Delta t_{i,j}/V_{i,j}\left(F^{n}_{i+1/2,j} - F^{n}_{i-1/2,j}\right); \quad (41)$$

$$Q^{*}_{i,j} = Q^{n}_{i,j} + \Delta Q^{*}_{i,j}; \quad (42)$$

and, in the final step, considering the η direction:

$$\Delta Q^{n+1}_{i,j} = -\Delta t_{i,j}/V_{i,j}\left(F^{*}_{i,j+1/2} - F^{*}_{i,j-1/2}\right); \quad (43)$$

$$Q^{n+1}_{i,j} = Q^{*}_{i,j} + \Delta Q^{n+1}_{i,j}. \quad (44)$$

The viscous vectors at the flux interface are obtained by arithmetical average between the primitive variables at the left and at the right states of the flux interface, as also arithmetical average of the primitive variable gradients. The gradients of the primitive variables present in the viscous flux vectors are calculated employing the Green Theorem which considers that the gradient of a primitive variable is constant in the volume and that the volume integral which defines this gradient is replaced by a surface integral ([26]); For instance, to $\partial u/\partial x$:

$$\frac{\partial u}{\partial x} = \frac{1}{V}\int_{V}\frac{\partial u}{\partial x}dV = \frac{1}{V}\int_{S} u\left(\vec{n}_x \bullet d\vec{S}\right) = \frac{1}{V}\int_{S_x} u dS_x \cong \frac{1}{V}\left[0.5\left(u_{i,j}+u_{i,j-1}\right)S_{x_{i,j-1/2}} + 0.5\left(u_{i,j}+u_{i+1,j}\right)S_{x_{i+1/2,j}} + 0.5\left(u_{i,j}+u_{i,j+1}\right)S_{x_{i,j+1/2}} + 0.5\left(u_{i,j}+u_{i-1,j}\right)S_{x_{i-1/2,j}}\right]. \quad (45)$$

4 Numerical Scheme of [14]

4.1 Explicit Upwind Algorithm

A typical conservative numerical scheme, using a finite volume formulation, for solving Eq. (1) can be expressed in terms of numerical fluxes as follows:

$$Q^{n+1}_{i,j} = Q^{n}_{i,j} - \Delta t_{i,j}/V_{i,j}\left(E^{N}_{i+1/2,j} - E^{N}_{i-1/2,j}\right) - \Delta t_{i,j}/V_{i,j}\left(F^{N}_{i,j+1/2} - F^{N}_{i,j-1/2}\right), \quad (46)$$

where $E^{N}_{i+1/2,j}$ and $F^{N}_{i,j+1/2}$ are the numerical fluxes. For a first order upwind scheme, $E^{N}_{i+1/2,j}$ is given by:

$$E^{N}_{i+1/2,j} = E^{n}_{i+1/2,j} - \hat{A}^{+}_{i+1/2,j}\Delta_{i+1/2,j}E^{n}_{i,j}, \quad (47)$$

with: $\Delta_{i+1/2,j} = (\cdot)_{i+1,j} - (\cdot)_{i,j}$, $E^{n}_{i+1/2,j}$ and $E^{n}_{i,j}$ defined by:

$$E^{n}_{i+1/2,j} = V_{\mathrm{int}}\begin{Bmatrix}\rho U_{cont}\\ \rho u U_{cont} + ph_x\\ \rho v U_{cont} + ph_y\\ (e+p)U_{cont}\end{Bmatrix}_{i+1/2,j} \quad \text{and}$$

$$E^{n}_{i,j} = V_{\mathrm{int}}\begin{Bmatrix}\rho U_{cont}\\ \rho u U_{cont} + ph_x\\ \rho v U_{cont} + ph_y\\ (e+p)U_{cont}\end{Bmatrix}_{i,j}; \quad (48)$$

and $\hat{A}^{+}_{i+1/2,j}$ defined as follows:

$$\hat{A}^{+}_{i+1/2,j} = \left(R_\xi \hat{\Lambda}^{+}_{\xi} R^{-1}_{\xi}\right)_{i+1/2,j},\ \hat{\Lambda}^{+}_{\xi} = diag\left\{\hat{\lambda}^{+}_{l}\right\} \quad \text{and}$$

$$\hat{\lambda}^{+}_{l} = 0.5\left[1 + sign\left(\lambda^{\xi}_{l}\right)\right], \quad (49)$$

where: R_ξ and R^{-1}_{ξ} are defined in [25; 27]; $diag(\cdot)$ represents a diagonal matrix, as for instance:

$$\hat{\Lambda}^{+}_{\xi} = \begin{bmatrix}\hat{\lambda}^{+}_{1} & & & \\ & \hat{\lambda}^{+}_{2} & & \\ & & \hat{\lambda}^{+}_{3} & \\ & & & \hat{\lambda}^{+}_{4}\end{bmatrix}; \quad (50)$$

λ^{ξ}_{l} are defined by Eqs. (21) and (22) to the ξ direction; and $sign\left(\lambda^{\xi}_{l}\right)$ is equal to 1.0 if $\lambda^{\xi}_{l} \geq 0.0$ and -1.0 otherwise. For explicit methods in the two-dimensional space, the Strang type directional splitting is employed:

$$Q^{n+2}_{i,j} = L_\xi(\Delta t)L_\eta(\Delta t)L_\eta(\Delta t)L_\xi(\Delta t)Q^{n}_{i,j}. \quad (51)$$

The L_ξ operator is defined by:

$$L_\xi(\Delta t)Q^{n}_{i,j} = Q^{n}_{i,j} - \Delta t_{i,j}\left(E^{N}_{i+1/2,j} - E^{N}_{i-1/2,j}\right). \quad (52)$$

Similar expressions can be given for $F^N_{i,j+1/2}$ and the L_η operator.

4.2 Uniformly Second Order Essentially Nonoscillatory Schemes

[3] proposed to construct second order accurate TVD schemes by applying a first order approximate Riemann solver to a modified flux. Following [3], [14] proposed to define a modified numerical flux function with the definition of the modified fluxes:

$$E^n = E^M = E^n + \overline{E}^n,\ F^n = F^M = F^n + \overline{F}^n, \quad (53)$$

where E^M and F^M are the modified fluxes which have essentially nonoscillatory property yet to be defined. In the following, a numerical method of uniformly second order accuracy in time and space which combines both characteristic and conversion features of Eq. (1) is discussed. For the present ENO scheme, the numerical flux E^N is described by:

$$E^N_{i+1/2,j} = E^M_{i+1,j} - \hat{A}^+_{\xi_{i+1/2,j}} \Delta_{i+1/2,j} E^M_{i,j} = E^M_{i,j} + \hat{A}^-_{\xi_{i+1/2,j}} \Delta_{i+1/2,j} E^M_{i,j}.$$

(54)

The components of the additional vector $\overline{E}$ are given by:

$$\bar{e}_{i,j} = m\left[\tilde{e}_{i-1/2,j} + \beta\overline{m}\left(\Delta_-\tilde{e}_{i-1/2,j}, \Delta_+\tilde{e}_{i-1/2,j}\right), \tilde{e}_{i+1/2,j} - \beta\overline{m}\left(\Delta_-\tilde{e}_{i+1/2,j}, \Delta_+\tilde{e}_{i+1/2,j}\right)\right],$$

(55)

where $\Delta_- = (\cdot)_{i,j} - (\cdot)_{i-1,j}$, $\Delta_+ = (\cdot)_{i+1,j} - (\cdot)_{i,j}$, and $\tilde{e}_{i+1/2,j}$ are components of the following column vector:

$$\tilde{E}_{i+1/2,j} = sign\left(A_{i+1/2,j}\right)\left(I - \Delta t_{i,j}\left|A_{i+1/2,j}\right|\right)\Delta_{i+1/2,j}\, E_{i,j}/2.$$

(56)

The $sign(A)$ and $|A|$ in Eq. (56) are given by:

$$sign(A) = R_\xi\, diag\left\{sign\left(\lambda^\xi_l\right)\right\}R^{-1}_\xi \text{ and } |A| = R_\xi\, diag\left\{\left|\lambda^\xi_l\right|\right\}R^{-1}_\xi.$$

(57)

Similar derivations can be given for the $\overline{F}$ vector in the η direction. In Equation (55), *m* is the minmod function:

$$m(a,b) = s \times \min\left(|a|, |b|\right), \quad \text{if } sign(a) = sign(b) = s; \quad (58)$$

$$m(a,b) = 0.0, \text{ otherwise.} \quad (59)$$

and the $\overline{m}$ function is defined by:

$$\overline{m} = a, \quad \text{if } |a| \le |b|; \quad (60)$$

$$\overline{m} = b, \quad \text{if } |a| \ge |b|. \quad (61)$$

For β = 0.0, one has a second order TVD scheme. For β = 0.5, one has a uniformly second order nonoscillatory scheme. The numerical scheme is thus formed by Eq. (46) using the definition (54) to the numerical flux function and the explicit time integration is performed by the Strang method described by Eqs. (51) and (52).

The present author introduced some modifications in the [14] schemes. Equation (54) is redefined as:

$$E^N_{i+1/2,j} = E^M_{i+1,j} - A^+_{\xi_{i+1/2,j}} \Delta_{i+1/2,j} Q^M_{i,j} = E^M_{i,j} + A^-_{\xi_{i+1/2,j}} \Delta_{i+1/2,j} Q^M_{i,j},$$

(62)

with: $E^M_{i+1,j} = E^n_{i+1,j} + A^n_{\xi_{i,j}} \overline{E}^n_{i+1,j}$ and $Q^M_{i,j} = V_{\text{int}}\{\rho \ \ \rho u \ \ \rho v \ \ e\}^T_{i,j} + \overline{E}^n_{i,j}$. The positive splitting matrix $A^+_{\xi_{i+1/2,j}}$ is defined as $A^+_{\xi_{i+1/2,j}} = R_\xi\, diag\left\{\lambda^+_l\right\}R^{-1}_\xi$, with $\lambda^+_l = 0.5\left(\lambda^\xi_l + \left|\lambda^\xi_l\right|\right)$, and the Jacobian matrix at the ξ direction is described by $A^n_{\xi_{i,j}} = R_\xi\, diag\left\{\lambda^\xi_l\right\}R^{-1}_\xi$. The vector $\tilde{E}_{i+1/2,j}$ is also redefined as:

$$\tilde{E}_{i+1/2,j} = sign\left(A_{i+1/2,j}\right)\left(I - \Delta t_{i,j}\left|A_{i+1/2,j}\right|\right)\Delta_{i+1/2,j}\, Q_{i,j}/2,$$

(63)

where $Q_{i,j} = V_{\text{int}}\{\rho \ \ \rho u \ \ \rho v \ \ e\}^T_{i,j}$, the vector of conserved variables. Observe that the resulting schemes are equivalent to the originals of [14], with the unique difference that the difference of fluxes in Eq. (56) is changed by the difference of conserved variables, Eq. (63). With this new definition, the solutions present better behavior, free of oscillations, undershoots and overshoots. The other expressions maintain the same structure.

The right-hand-side of the [14] schemes, necessaries to the resolution of the implicit version of this algorithm, is defined by:

$$\mathrm{RHS(Y)}^{n}_{i,j} = -\Delta t_{i,j}/\mathrm{V}_{i,j}\left(\mathrm{E}^{N}_{i+1/2,j} - \mathrm{E}^{N}_{i-1/2,j} + \mathrm{F}^{N}_{i,j+1/2} - \mathrm{F}^{N}_{i,j-1/2}\right). \quad (64)$$

The explicit version of this algorithm to perform the viscous simulations is described by Eqs. (51) and (52). The implementation of the viscous terms follows the same procedure as described in section 3.

5 Implicit Formulation

All implicit schemes implemented in this work used backward Euler in time and ADI approximate factorization to solve a three-diagonal system in each direction.

5.1 Approximate Factorization ADI – [6] TVD Scheme

The ADI approximate factorization form to the implicit scheme of [6] is presented in two stages, each one associated with a different coordinate direction:

$$\left[I + \Delta t_{i,j}\Delta^{\xi}_{+}J^{-}_{i+1/2,j} + \Delta t_{i,j}\Delta^{\xi}_{-}J^{+}_{i+1/2,j}\right]\Delta Q^{*}_{i,j} = RHS_{i,j}; \quad (65)$$

$$\left[I + \Delta t_{i,j}\Delta^{\eta}_{+}K^{-}_{i,j+1/2} + \Delta t_{i,j}\Delta^{\eta}_{-}K^{+}_{i,j+1/2}\right]\Delta Q^{n+1}_{i,j} = \Delta Q^{*}_{i,j}, \quad (66)$$

where: $RHS_{i,j}$ is defined by Eq. (40); the difference operators are defined as:

$$\Delta^{\xi}_{+}(\cdot) = (\cdot)_{i+1,j} - (\cdot)_{i,j}, \ \Delta^{\xi}_{-}(\cdot) = (\cdot)_{i,j} - (\cdot)_{i-1,j}, \quad (67)$$

$$\Delta^{\eta}_{+}(\cdot) = (\cdot)_{i,j+1} - (\cdot)_{i,j}, \ \Delta^{\eta}_{-}(\cdot) = (\cdot)_{i,j} - (\cdot)_{i,j-1}, \quad (68)$$

and the update of the conserved variable vector is proceeded as follows:

$$Q^{n+1}_{i,j} = Q^{n}_{i,j} + \Delta Q^{n+1}_{i,j}. \quad (69)$$

This system of 4x4 block three-diagonal linear equations is solved using LU decomposition and the Thomas algorithm applied to systems of block matrices. The splitting matrices J^{+}, J^{-}, K^{+} and K^{-} are defined as:

$$J^{+} = R_{\xi}\Lambda^{+}_{\xi}R^{-1}_{\xi}, \ J^{-} = R_{\xi}\Lambda^{-}_{\xi}R^{-1}_{\xi}, \ K^{+} = R_{\eta}\Lambda^{+}_{\eta}R^{-1}_{\eta}; \quad (70)$$

$$K^{-} = R_{\eta}\Lambda^{-}_{\eta}R^{-1}_{\eta} \quad (71)$$

The diagonal matrices of eigenvalues are determined, for instance, by:

$$\Lambda^{+}_{\xi} = \begin{bmatrix} \lambda^{\xi,+}_{1} & & & \\ & \lambda^{\xi,+}_{2} & & \\ & & \lambda^{\xi,+}_{3} & \\ & & & \lambda^{\xi,+}_{4} \end{bmatrix} \text{ and } \Lambda^{-}_{\xi} = \begin{bmatrix} \lambda^{\xi,-}_{1} & & & \\ & \lambda^{\xi,-}_{2} & & \\ & & \lambda^{\xi,-}_{3} & \\ & & & \lambda^{\xi,-}_{4} \end{bmatrix}, \quad (72)$$

with: $\lambda^{\xi,+}_{l} = 0.5\left(\lambda^{\xi}_{l} + \left|\lambda^{\xi}_{l}\right|\right)$; $\lambda^{\xi,-}_{l} = 0.5\left(\lambda^{\xi}_{l} - \left|\lambda^{\xi}_{l}\right|\right)$; and R_{ξ} and R^{-1}_{ξ} defined in [25;27]. Similar expressions are valid to the η direction. This implicit formulation to the LHS of the [6] scheme is first order accurate in time and space. The solution accuracy in space in the state steady condition is of second order due to the RHS.

5.2 Approximate Factorization ADI – [14] TVD/ENO Schemes

The implicit scheme in ADI approximate factorization form is given by:

$$\left[I + \Delta t_{i,j}\hat{A}^{+}_{i-1/2,j}\Delta_{-}A_{\xi_{i,j}} + \Delta t_{i,j}\hat{A}^{-}_{i+1/2,j}\Delta_{+}A_{\xi_{i,j}}\right]\Delta Q^{*}_{i,j} = RHS_{i,j}; \quad (73)$$

$$\left[I + \Delta t_{i,j}\hat{B}^{+}_{i,j-1/2}\Delta_{-}B_{\eta_{i,j}} + \Delta t_{i,j}\hat{B}^{-}_{i,j+1/2}\Delta_{+}B_{\eta_{i,j}}\right]\Delta Q^{n+1}_{i,j} = \Delta Q^{*}_{i,j}, \quad (74)$$

where $RHS_{i,j}$ is defined by Eq. (64) and the matrices above are defined as follows:

$$\hat{A}^{+}_{i-1/2,j} = \left[T_{\xi}\,diag\left\{\hat{\lambda}^{\xi,+}_{l}\right\}T^{-1}_{\xi}\right]_{i-1/2,j} \quad \text{and}$$

$$\hat{\mathrm{A}}^{-}_{\mathrm{i+1/2,j}} = \left[\mathrm{T}_{\xi}\,\mathrm{diag}\left\{\hat{\lambda}^{\xi,-}_{\mathrm{l}}\right\}\mathrm{T}^{-1}_{\xi}\right]_{\mathrm{i+1/2,j}}; \quad (75)$$

$$\hat{B}^{+}_{i,j-1/2} = \left[T_{\eta}\,diag\left\{\hat{\lambda}^{\eta,+}_{l}\right\}T^{-1}_{\eta}\right]_{i,j-1/2}, \quad \text{and}$$

$$\hat{B}^{-}_{i,j+1/2} = \left[T_{\eta}\,diag\left\{\hat{\lambda}^{\eta,-}_{l}\right\}T^{-1}_{\eta}\right]_{i,j+1/2}; \quad (76)$$

$$A_{\xi_{i,j}} = \left[T_{\xi}\,diag\left\{\lambda^{\xi}_{l}\right\}T^{-1}_{\xi}\right]_{i,j} \text{ and } B_{\eta_{i,j}} = \left[T_{\eta}\,diag\left\{\lambda^{\eta}_{l}\right\}T^{-1}_{\eta}\right]_{i,j}, \quad (77)$$

with:

$$\hat{\lambda}^{\xi,+}_{l} = 0.5\left[1 + sign\left(\lambda^{\xi}_{l}\right)\right], \ \hat{\lambda}^{\xi,-}_{l} = 0.5\left[1 - sign\left(\lambda^{\xi}_{l}\right)\right]; \quad (78)$$

$$\hat{\lambda}^{\eta,+}_{l} = 0.5\left[1 + sign\left(\lambda^{\eta}_{l}\right)\right], \ \hat{\lambda}^{\eta,-}_{l} = 0.5\left[1 - sign\left(\lambda^{\eta}_{l}\right)\right]; \quad (79)$$

and the similar transformation matrix T and its inverse specified in [27].

This implicit formulation to the LHS of the [14] schemes is first order accurate in time and space. The solution accuracy in space in the state steady condition is of second order due to the RHS.

6 Turbulence Models

The turbulence models of [15] and of [16] are described in [28-29]. The [17] model is described as follows.

6.1 Turbulence Model of [17]

Aiming to overcome the limitations of algebraic models and to avoid the difficulties of the implementation of two-equation models or of Reynolds stress ones, the one-equation model of [17], involving the transport of eddy viscosity, is implemented. This model was chosen due to the reasonable results obtained in a large range of flows and due to its numerical properties. This model takes naturally into account the effects of the turbulence history and of diffusion.

The transport equation to the work turbulent kinematic viscosity is described by:

$$\frac{D\tilde{\nu}}{Dt} = c_{b1}\tilde{S}\tilde{\nu} + \frac{1}{\sigma}\left[\nabla\bullet\left((\nu+\tilde{\nu})\nabla\tilde{\nu}\right) + c_{b2}(\nabla\tilde{\nu})^2\right] - c_{w1}f_w(r)\left(\frac{\tilde{\nu}}{N}\right)^2. \quad (80)$$

In this equation, the first term of the right hand side is the production term of work kinematic viscosity, the second term is the diffusion term of viscosity and the last one is the destruction term, or dissipation term, of work kinematic viscosity.

The turbulent viscosity is defined by:

$$\mu_T = \rho\tilde{\nu}f_{v1}. \quad (81)$$

With the intention to assure that $\tilde{\nu}$ matches $K\times N\times\sqrt{\tau_{xy,w}/\rho_w}$ at the logarithmic layer and at the viscous sub-layer, the damping function f_{v1} is defined by:

$$f_{v1} = \lambda^3/\left(\lambda^3 + c_{v1}^3\right) \quad (82)$$

as function of the variable $\lambda = \tilde{\nu}/\nu$. The function $\tilde{S}$ is determined by the expression:

$$\tilde{S} = |\partial u/\partial y| + \left[\tilde{\nu}/(\kappa N)^2\right]f_{v2}, \quad (83)$$

where f_{v2} has the following expression:

$$f_{v2} = 1 - \lambda/(1+\lambda f_{v1}). \quad (84)$$

The destruction term should disappear at the external region of the boundary layer. [17] suggest the following function to make possible such behavior:

$$f_w(r) = g\left[\left(1+c_{w3}^6\right)/\left(g^6+c_{w3}^6\right)\right]^{1/6},\ g = r + c_{w2}\left(r^6 - r\right); \quad (85)$$

$$r = \tilde{\nu}/\left[(\kappa N)^2\tilde{S}\right], \quad (86)$$

with the argument r and the function f_w reaching the value 1.0 at the logarithmic layer and decreasing at the external region. The function g is merely a limiter to avoid high values of f_w. The [17] constants have the following values:

$$c_{b1} = 0.1355,\ c_{b2} = 0.622,\ c_{w2} = 0.3,\ c_{v1} = 7.1,\ \sigma = 2/3,\ c_{w3} = 2.0;$$

$$c_{w1} = \frac{c_{b1}}{\kappa^2} + \frac{(1+c_{b2})}{\sigma}.$$

This model is marched in time employing the implicit method LU-SGS (Lower-Upper Factorization – Symmetrical Gauss-Seidel). Details of such implicit implementation in two-dimensions can be found in [17]. In the present work, the term relative to the diffusion of work kinematic viscosity was not implemented. The studied model considers only the production and dissipation terms of work kinematic viscosity.

Initial and boundary conditions to solve the differential equation are reported in [17].

7 Spatially Variable Time Step

The basic idea of this procedure consists in keeping constant the CFL number in all calculation domain, allowing, hence, the use of appropriated time steps to each specific mesh region during the convergence process. Two models, each one associated to the respective type of flow, are described.

7.1 Inviscid Model

According to the definition of the CFL number, it is possible to write:

$$\Delta t_{i,j} = CFL(\Delta s)_{i,j}/c_{i,j}, \quad (87)$$

where CFL is the "Courant-Friedrichs-Lewy" number to provide numerical stability to the scheme; $c_{i,j} = \left[\sqrt{u^2+v^2}+a\right]_{i,j}$ is the maximum characteristic speed of propagation of information in the calculation domain; and $(\Delta s)_{i,j}$ is a characteristic

length of transport of information. On a finite volume context, $(\Delta s)_{i,j}$ is chosen as the minor value found between the minor centroid distance, involving the *(i,j)* cell and a neighbor, and the minor cell side length.

7.2 Viscous Model

In this model, the time step is defined according to [30] work:

$$\Delta t_{i,j} = \left[\frac{CFL\left(\Delta t_c \Delta t_v\right)}{\Delta t_c + \Delta t_v} \right]_{i,j}, \qquad (88)$$

with Δt_c being the convective time step and Δt_v being the viscous time step. These quantities are defined as:

$$\left(\Delta t_c\right)_{i,j} = \frac{V_{i,j}}{\left(\lambda_c\right)_{i,j}}; \qquad (89)$$

$$\left(\lambda_c\right)_{i,j} = \max\left(\lambda^{\max}_{i,j-1/2}, \lambda^{\max}_{i+1/2,j}, \lambda^{\max}_{i,j+1/2}, \lambda^{\max}_{i-1/2,j}\right); \qquad (90)$$

$$\left(\lambda^{\max}\right)_{\text{int}} = \left(\left|u_{\text{int}} n_x + v_{\text{int}} n_y\right| + a_{\text{int}}\right) S_{\text{int}}; \qquad (91)$$

$$\left(\Delta t_v\right)_{i,j} = K_v \frac{V_{i,j}}{\left(\lambda_v\right)_{i,j}}, \quad \left(p1\right)_{i,j} = \frac{\gamma^{3/2} M_\infty}{\left(\text{Re}\,\text{Pr}\, d_L\right) V_{i,j}}; \qquad (92)$$

$$\left(p2\right)_{i,j} = \frac{\mu_{i,j-1/2}}{\rho_{i,j-1/2}} S^2_{i,j-1/2} + \frac{\mu_{i+1/2,j}}{\rho_{i+1/2,j}} S^2_{i+1/2,j} + \frac{\mu_{i,j+1/2}}{\rho_{i,j+1/2}} S^2_{i,j+1/2} + \frac{\mu_{i-1/2,j}}{\rho_{i-1/2,j}} S^2_{i-1/2,j}; \qquad (93)$$

$$\left(\lambda_v\right)_{i,j} = \left(p1 \times p2\right)_{i,j}, \qquad (94)$$

where interface properties are calculated by arithmetical average, M_∞ is the freestream Mach number and K_v is equal to 0.25, as recommended by [30].

8 Configurations of the Physical Problems, Employed Meshes and Initial and Boundary Conditions

8.1 Computational Cell, Configurations and Meshes

In this section, the computational cell employed in the numerical experiments and the physical configurations at the xy plane of the studied problems in this work are described altogether with the employed mesh in each case (inviscid and laminar and turbulent).

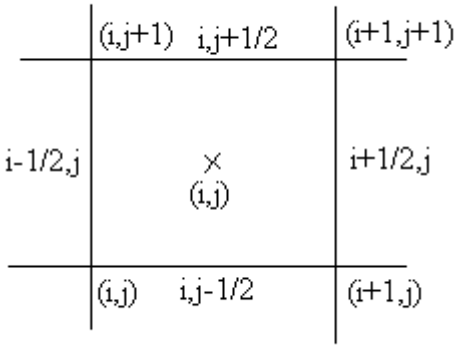

Figure 1. Computational cell.

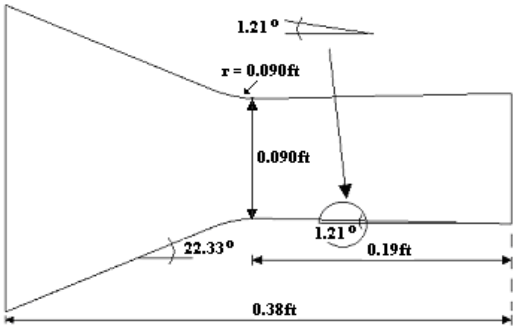

Figure 2. Nozzle configuration in the xy plane.

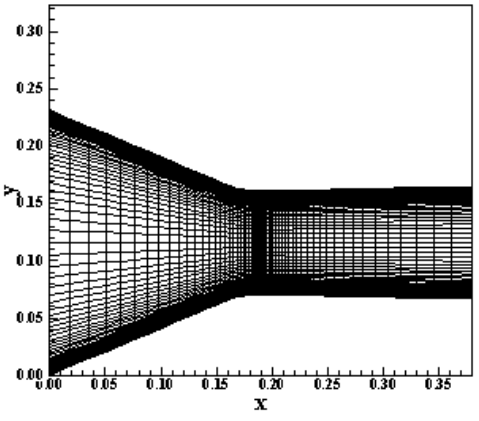

Figure 3. Nozzle mesh in two-dimensions.

Figure 1 describes the computational cell. The geometry of the convergent-divergent nozzle at the xy plane is described in Fig. 2. The total length of the nozzle is 0.38ft (0.116m) and the throat height is equal to 0.090ft (0.027m). The throat is located at 0.19ft (0.058m) from the entrance boundary. The throat curvature ratio is equal to 0.090ft. The nozzle convergence angle is 22.33° and the nozzle

divergence angle is 1.21°. An exponential stretching of 10% in both ξ and η directions was used. An algebraic mesh of 61 points in the ξ direction and 71 points in the η direction was generated, which corresponds in finite volumes to 4,200 rectangular cells and 4,331 nodes. Figure 3 exhibits the mesh employed in the simulations.

The compression corner configuration at the xy plane is described in Fig. 4. The corner inclination angle is 10^o. An algebraic mesh of 70 points in the ξ direction and 50 points in the η direction was generated, which corresponds in finite volumes to 3,381 rectangular cells and 3,500 nodes. Figure 5 exhibits such mesh.

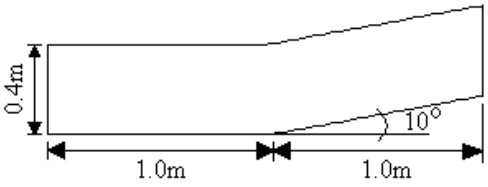

Figure 4. Corner configuration in the xy plane.

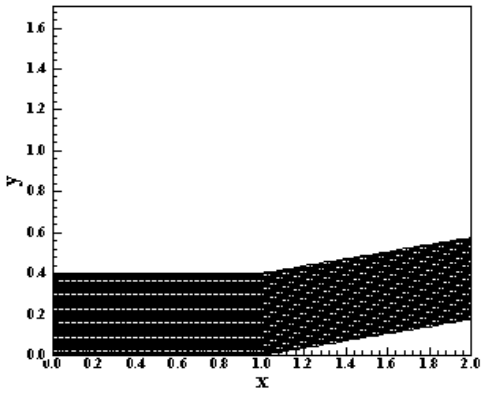

Figure 5. Corner mesh in two-dimensions.

Finally, the ramp configuration at the xy plane is described in Fig. 6. The compression corner has 20° of inclination. The mesh used in the simulations has 3,540 rectangular cells and 3,660 nodes to a structured discretization of the calculation domain. This mesh is equivalent, in finite differences, of being composed of 61 points in the ξ direction and 60 points in the η direction. An exponential stretching of 10% in the η direction was employed. Figure 7 shows such mesh.

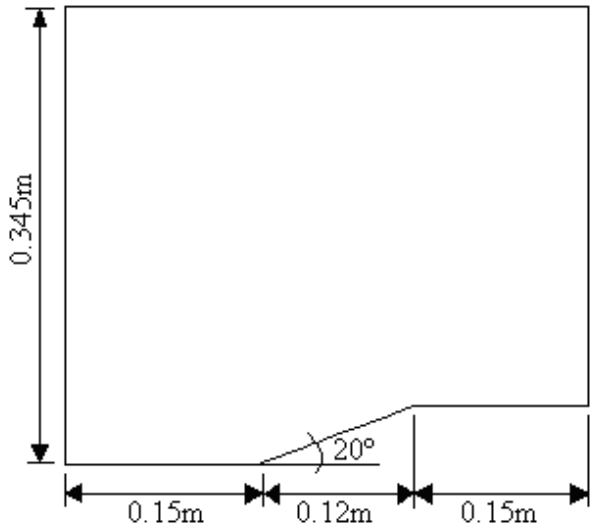

Figure 6. Ramp configuration in the xy plane.

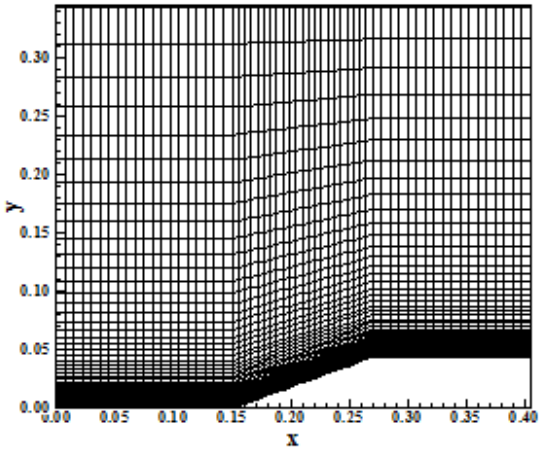

Figure 7. Ramp mesh in two-dimensions.

8.2 Initial Conditions

Stagnation values are used as initial condition to the nozzle problem. Only at the exit boundary is imposed a reduction of 1/3 to the density and to the pressure to start the flow along the nozzle. The vector of conserved variables is defined as:

a) Domain except the nozzle exit:

$$Q = \{1 \quad 0 \quad 0 \quad (\gamma+1)/[2\gamma(\gamma-1)]\}^t ; \qquad (95)$$

b) Nozzle exit:

$$Q = \{1/3 \quad 0 \quad 0 \quad (\gamma+1)/[6\gamma(\gamma-1)]\}^t . \qquad (96)$$

To the others problems, values of freestream flow are adopted for all properties as initial condition, in the whole calculation domain:

$$Q_\infty = \{1 \quad M_\infty \cos\theta \quad M_\infty sen\theta \quad [1/[\gamma(\gamma-1)]+0.5M_\infty^2]\}^t , \qquad (97)$$

where M_∞ represents the freestream Mach number and θ is the flow attack angle.

8.3 Boundary Conditions

The boundary conditions are basically of three types: solid wall, entrance and exit. These conditions are implemented in special cells named ghost cells.

(a) Wall condition: This condition imposes the flow tangency at the solid wall to the inviscid case. This condition is satisfied considering the wall tangent velocity component of the ghost volume as equals to the respective velocity component of its real neighbor cell. At the same way, the wall normal velocity component of the ghost cell is equaled in value, but with opposite signal, to the respective velocity component of the real neighbor cell.

The pressure gradient normal to the wall is assumed be equal to zero, following an inviscid formulation. The same hypothesis is applied to the temperature gradient normal to the wall, considering adiabatic wall. The ghost volume density and pressure are extrapolated from the respective values of the real neighbor volume (zero order extrapolation), with these two conditions. The total energy is obtained by the state equation of a perfect gas.

To the viscous case, only the velocity components are determined in a different way from the inviscid case. This condition is satisfied considering the wall tangent velocity component of the ghost volume as equals to the respective velocity component of its real neighbor cell, with opposite signal. At the same way, the wall normal velocity component of the ghost cell is equaled in value, but also with opposite signal, to the respective velocity component of the real neighbor cell.

The pressure gradient normal to the wall is assumed be equal to zero, following the boundary layer theory. The same hypothesis is applied to the temperature gradient normal to the wall, considering adiabatic wall. The ghost volume density and pressure are extrapolated from the respective values of the real neighbor volume (zero order extrapolation), with these two conditions. The total energy is obtained by the state equation of a perfect gas.

(b) Entrance condition:

(b.1) Subsonic flow: Three properties are specified and one is extrapolated, based on analysis of information propagation along characteristic directions in the calculation domain ([31]). In other words, three characteristic directions of information propagation point inward the computational domain and should be specified. Only the characteristic direction associated to the "(q_n-a)" velocity cannot be specified and should be determined by interior information of the calculation domain. The u velocity component was the extrapolated variable from the real neighbor volume to the nozzle problem, while the pressure was the extrapolated variable to the others problems. Density and pressure had their values determined by isentropic relations in the nozzle problem, while density and velocity components had their values determined by the freestream flow properties in the others problems. The total energy per unity fluid volume is determined by the state equation of a perfect gas.

(b.2) Supersonic flow: All variables are fixed with their freestream flow values.

(c) Exit condition:

(c.1) Subsonic flow: Three characteristic directions of information propagation point outward the computational domain and should be extrapolated from interior information ([31]). The characteristic direction associated to the "(q_n-a)" velocity should be specified because it penetrates the calculation domain. In this case, the ghost volume's pressure is specified by its freestream value. Density and velocity components are extrapolated and the total energy is obtained by the state equation of a perfect gas.

(c.2) Supersonic flow: All variables are extrapolated from the interior domain due to the fact that all four characteristic directions of information propagation of the Euler equations point outward the calculation domain and, with it, nothing can be fixed.

9 Results

Tests were performed in a microcomputer with processor AMD SEMPRON (tm) 2600+, 1.83GHz, and 512 Mbytes of RAM memory. The criterion adopted in this work to obtain convergence considers a reduction of 3 orders in the magnitude of the maximum residual in the domain, a typical criterion in the CFD community. In all problems, the entrance angle was set equal to 0.0°. To the inviscid cases, the implicit formulation was employed to generate the numerical results, whereas to the viscous laminar and turbulent cases, the explicit version was used.

9.1 Inviscid Results

9.1.1 Convergent-Divergent Nozzle

Stagnation flow was adopted as initial condition to this problem. Figures 8 to 10 show the pressure contours obtained by the [6], the [14]/TVD, and the [14]/ENO schemes, respectively. All schemes presented the same quantitative pressure field. Good symmetry characteristics are observed in all solutions.

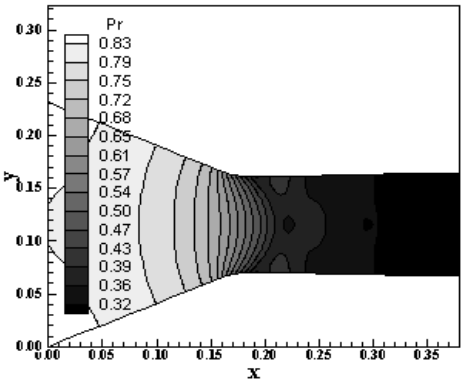

Figure 8. Pressure contours ([6]).

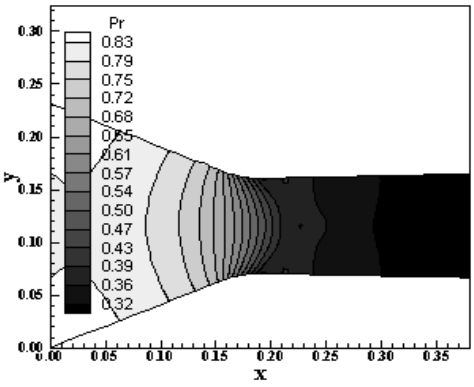

Figure 9. Pressure contours ([14]/TVD).

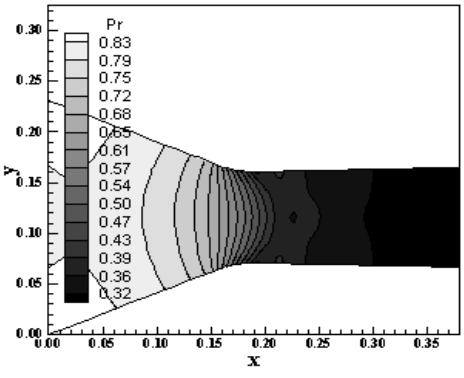

Figure 10. Pressure contours ([14]/ENO).

Figure 11 exhibits the lower wall pressure distributions along the convergent-divergent nozzle. They are compared with the experimental results of [32]. As can be observed, the [6] TVD scheme presents the best pressure distribution (closer to the experimental data).

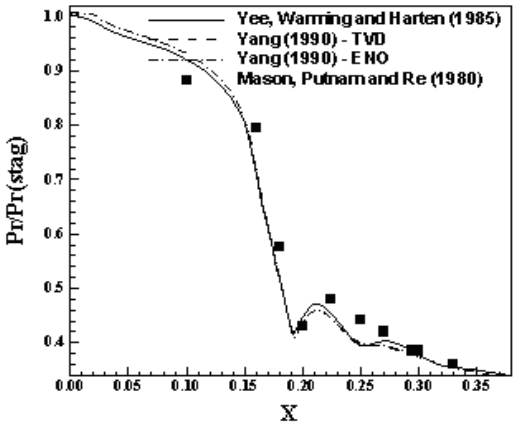

Figure 11. Wall pressure distributions.

9.1.2 Compression Corner

A freestream Mach number of 3.0, characterizing a moderate supersonic flow regime, was adopted as initial condition to this problem. The flow reaches the compression corner, generating an oblique shock wave along the corner. Figures 12 to 14 exhibit the pressure contours obtained by the schemes of [6], of [14]/TVD, and of [14]/ENO, respectively. The most severe pressure field after the oblique shock wave is obtained by the [6] TVD scheme. All solutions are clear, without pressure oscillations.

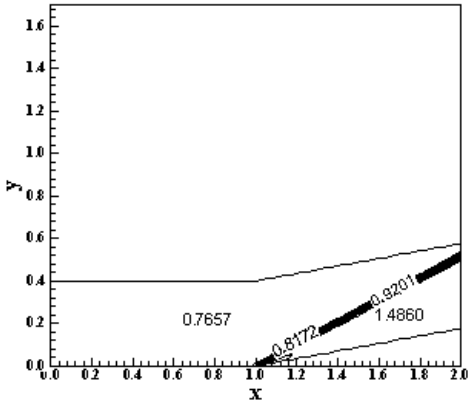

Figure 12. Pressure contours ([6]).

Figure 15 exhibits the wall pressure distributions along the compression corner obtained by all schemes. They are compared with the oblique shock wave theory results. As can be observed, the [6] TVD scheme presents oscillations at the discontinuity, originating a pressure peak at the corner. The [14]/TVD and [14]/ENO schemes present smooth transition at the shock wave, highlighting the good behavior of the ENO scheme as yielding an essentially non-oscillatory solution at

extrema. All schemes slightly under-predict the shock plateau. Figure 16 shows the same pressure distributions plotted using symbols to identify how much cells are necessary to capture the shock discontinuity. All schemes detect the shock discontinuity using four cells, which is a good number of cells in terms of high resolution schemes.

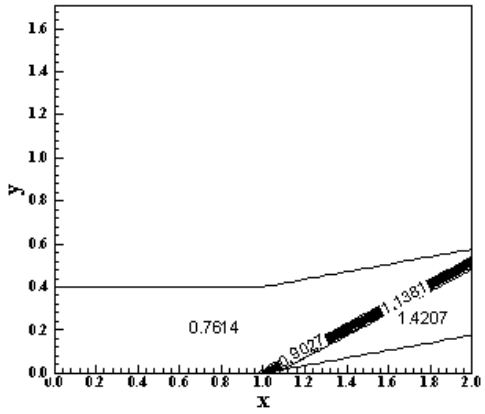

Figure 13. Pressure contours ([14]/TVD).

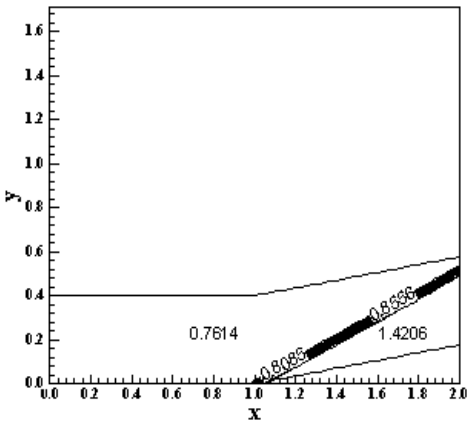

Figure 14. Pressure contours ([14]/ENO).

One way to quantitatively verify if the solutions generated by each scheme are satisfactory consists in determining the shock angle of the oblique shock wave, β, measured in relation to the initial direction of the flow field. [33] (pages 352 and 353) presents a diagram with values of the shock angle, β, to oblique shock waves. The value of this angle is determined as function of the freestream Mach number and of the deflection angle of the flow after the shock wave, ϕ. To the compression corner problem, ϕ = 10º (ramp inclination angle) and the freestream Mach number is 3.0, resulting from this diagram a value to β equals to 27.5º. Using a transfer in Figures 12 to 14, it is possible to obtain the values of β to each scheme, as well the respective errors, shown in Tab. 1. As can be observed, the best scheme was the Yang/ENO (1990) one, with a percentage error of 0.36%.

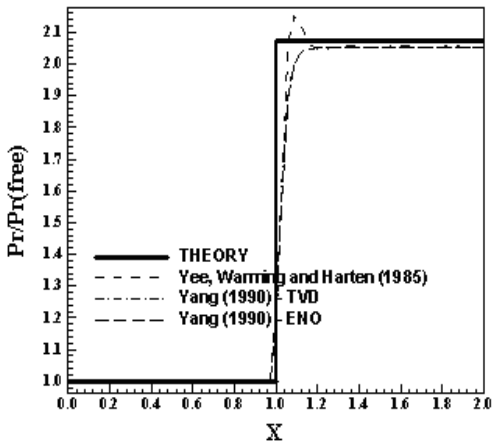

Figure 15. Wall pressure distributions.

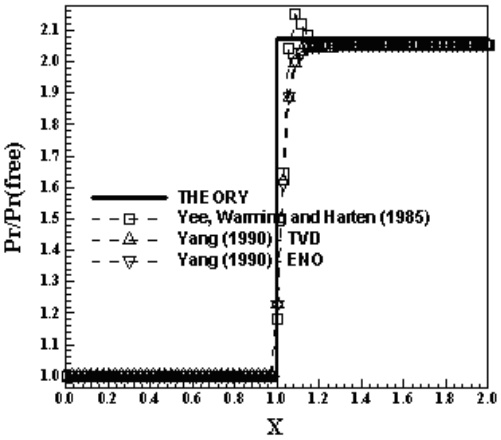

Figure 16. Wall pressure distributions.

Table 3. Shock angle and respective percentage errors to the corner problem.

Algorithm	β (°)	Error (%)
[6]	28.0	1.82
[14]/TVD	27.8	1.09
[14]/ENO	27.6	0.36

9.2 Viscous Results

The physical problem studied in the viscous laminar and turbulent simulations is the flow along a ramp. This problem is a low supersonic flow hitting a ramp with 20° of inclination. It generates a shock and an expansion fan. A boundary layer is also formed along the ramp wall. The freestream Mach number adopted as initial condition to this simulation was 2.0. The Reynolds number was estimated to be 1.613×10^5 at a flight altitude of 20,000m and l = 0.0437m, based on the work of [22]. To this Mach number and Reynolds number, a

separated flow is formed at the ramp wall, with the formation of a circulation bubble. This behavior is observed in all solutions of all schemes.

9.2.1 Laminar Viscous Results

Figures 17 to 19 exhibit the pressure contours obtained by the [6], the [14]/TVD, and the [14]/ENO schemes, respectively. The most severe pressure field, which characterizes the most conservative solution, is obtained by the [14]/ENO scheme. The shock wave is better captured by the [14] schemes. All schemes detect a weak shock wave formed ahead of the ramp's corner. This shock is due to the meaningful increase in the thickness of the boundary layer, which simulates a thicker geometry to the flow. This increase in the boundary layer thickness is originated by its separation, resulting in a circulation bubble, highlighted in Figs. 20 to 22.

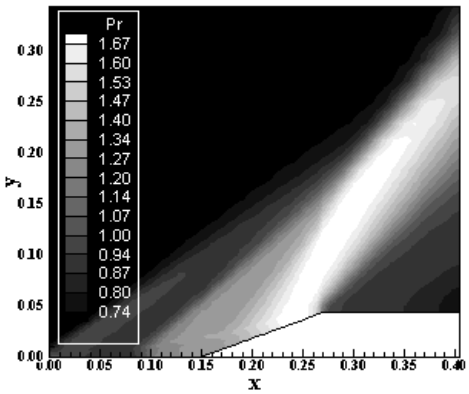

Figure 17. Pressure contours ([6]).

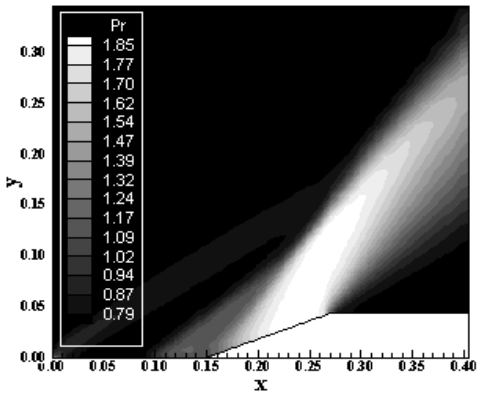

Figure 18. Pressure contours ([14]/TVD).

Figures 20 to 22 show the velocity vector fields close to the ramp wall and the respective streamlines obtained by the [6], by the [14]/TVD, and by the [14]/ENO schemes. It is possible to note regions of separated flow in the solutions generated by all schemes. The streamlines highlight this separated flow close to the wall, as well the formation of a circulation bubble. The separation region detected by the [6] TVD scheme is shorter than the respective ones detected by the [14]/TVD and [14]/ENO schemes. Nonethless, a thicker boundary layer is characterized in this case. The effect of the increase of the boundary layer thickness tends to yield a weaker shock ahead of the ramp, as mentioned in the pressure field analyses, detected by all schemes.

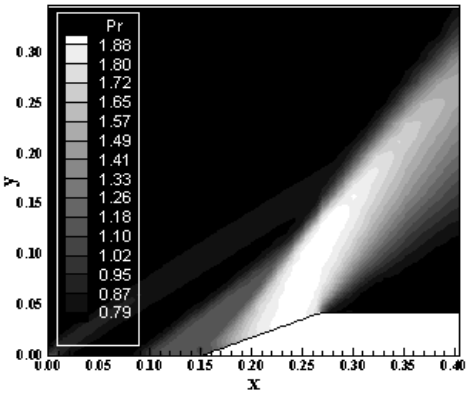

Figure 19. Pressure contours (Yang/ENO).

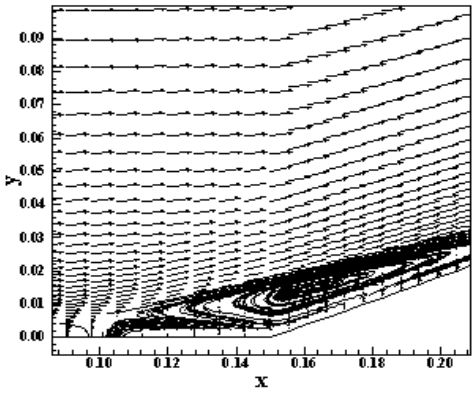

Figure 20. Velocity field and streamlines ([6]).

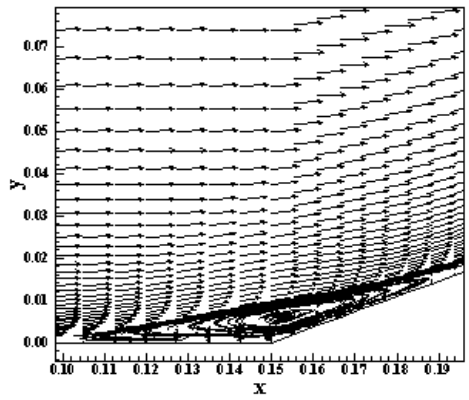

Figure 21. Velocity field and streamlines ([14]/TVD).

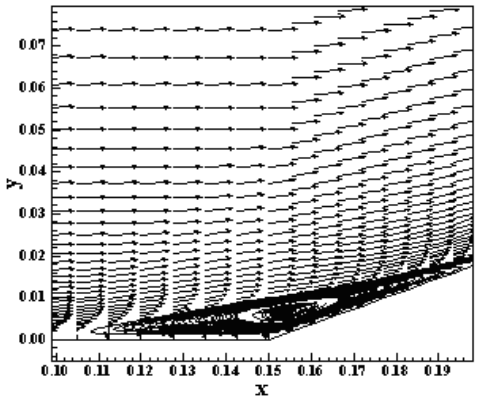

Figure 22. Velocity field and streamlines ([14]/ENO).

Figure 23 exhibits the wall pressure distributions obtained by all schemes. They are compared with inviscid solution, which represents the correct solution considering the boundary layer theory. The oblique shock wave and the Prandtl-Meyer expansion fan theories were applied to define the inviscid solution. All schemes present a small peak of pressure ahead of the ramp's corner, which defines the weaker shock (approximately at x = 0.125m). Better solutions are obtained by the [14]/TVD and [14]/ENO schemes, with pressure peaks, at the ramp region, closer to the pressure plateau of the inviscid solution. Both schemes under-predict the pressure plateau. The pressure after the expansion fan is also better captured by the versions of the [14] scheme.

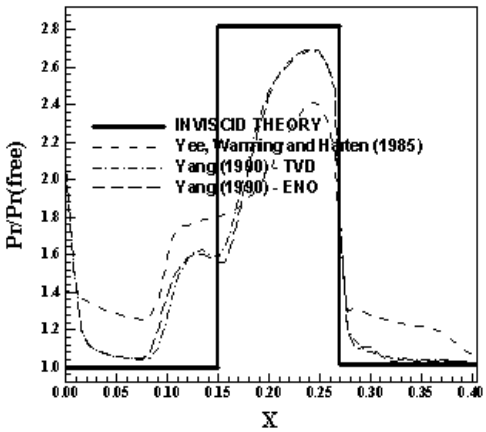

Figure 23. Wall pressure distributions (Lam).

Again, one way to quantitatively verify if the solutions generated by each scheme are satisfactory consists in determining the shock angle of the oblique shock wave, β, measured in relation to the initial direction of the flow field. To the ramp problem, $\phi = 20^o$ (ramp inclination angle) and the freestream Mach number is 2.0, resulting from this diagram a value to β equals to 53.0º. Using a transfer in Figures 17 to 19, it is possible to obtain the values of β to each scheme, as well the respective errors, shown in Tab. 4. As can be observed, the [6] and the [14]/ENO schemes present the best solutions, with an error of 2.83%.

Table 4. Shock angle and respective percentage errors to the ramp problem (Laminar).

Algorithm	β (°)	Error (%)
[6]	51.5	2.83
[14]/TVD	51.3	3.21
[14]/ENO	51.5	2.83

9.2.2 Turbulent Viscous Results

[15] ***Results.*** Figures 24 to 26 exhibit the pressure contours obtained by the [6], the [14]/TVD, and the [14]/ENO schemes, respectively, using the [15] turbulence model. The most severe pressure field, which characterizes the most conservative solution, is again obtained by the [14]/ENO scheme. The shock wave is better captured by the [14] schemes. All schemes detect the weak shock wave formed ahead of the ramp's corner described in the laminar case, with less extension and intensity because the effect of the turbulence model is to proportionate a more stable boundary layer. This shock is due to the meaningful increase in the thickness of the boundary layer, which simulates a thicker geometry to the flow. This increase in the boundary layer thickness is originated by its separation, resulting in a circulation bubble, highlighted in Figs. 27 to 29. As aforementioned, the effect of the turbulence model is to stabilize the boundary layer, originating a less extension region of separated flow.

Figures 27 to 29 show the velocity vector fields close to the ramp wall and the respective streamlines obtained by the [6], by the [14]/TVD, and by the [14]/ENO schemes using the [15] turbulence model. It is possible to note regions of separated flow in the solutions generated by all schemes. The streamlines highlight this separated flow close to the wall, as well the formation of a circulation bubble. The separation region detected by the [6] TVD scheme is longer than the respective ones detected by the [14]/TVD and [14]/ENO schemes. It also results in a thicker boundary layer captured by the [6] TVD scheme.

Figure 30 exhibits the wall pressure distributions obtained by all schemes using the [15] turbulence model. They are compared with inviscid solution, which represents the correct solution considering the

boundary layer theory. Better solutions are obtained by the [14]/TVD and [14]/ENO schemes, with pressure peaks, at the ramp region, closer to the pressure plateau of the inviscid solution. All three schemes under-predict the pressure plateau. The pressure after the expansion fan is also better captured by the versions of the [14] scheme.

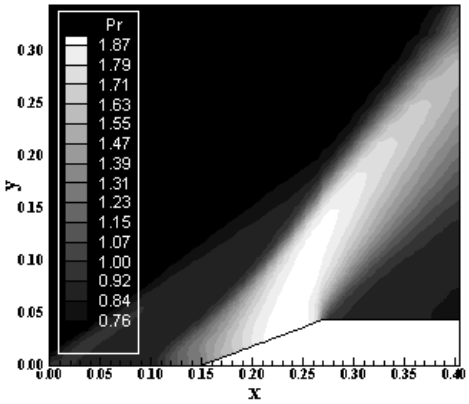

Figure 24. Pressure contours ([6]).

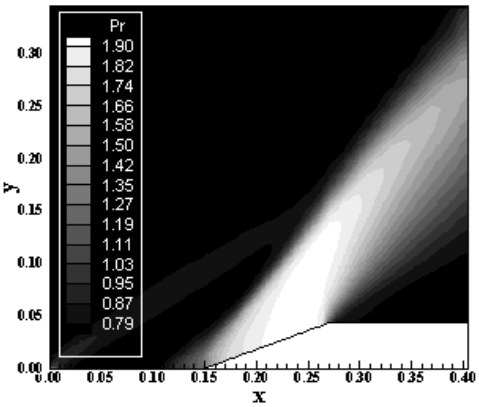

Figure 25. Pressure contours ([14]/TVD).

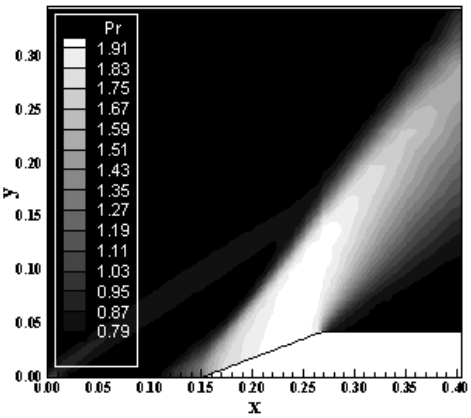

Figure 26. Pressure contours ([14]/ENO).

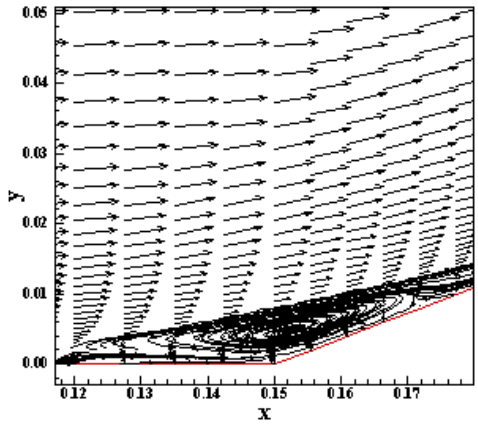

Figure 27. Velocity field and streamlines ([6]).

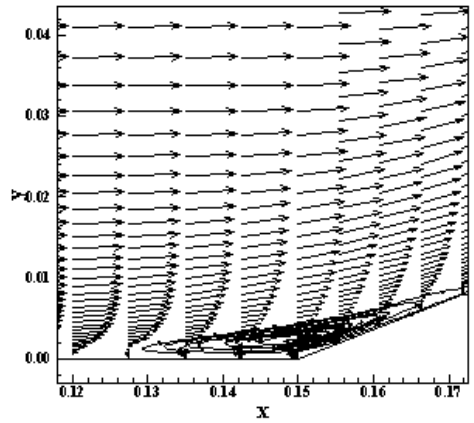

Figure 28. Velocity field and streamlines ([14]/TVD).

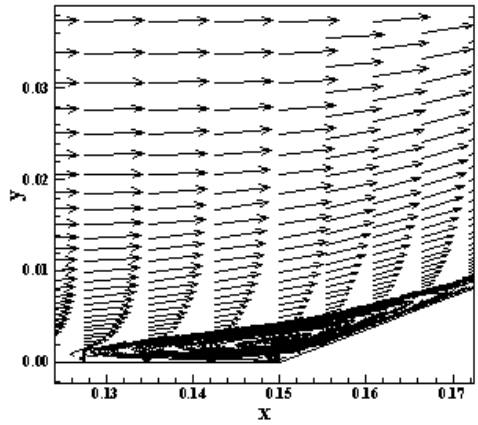

Figure 29. Velocity field and streamlines ([14]/ENO).

Again, it is possible to determine by each scheme the shock angle of the oblique shock wave, β, measured in relation to the initial direction of the flow field. Using a transfer in Figures 24 to 26, it is possible to obtain the values of β for each scheme, as well the respective errors, shown in Tab. 5. As can be observed, the best scheme employing the

[15] turbulence model was the [14]/TVD scheme, with an error of 0.38%.

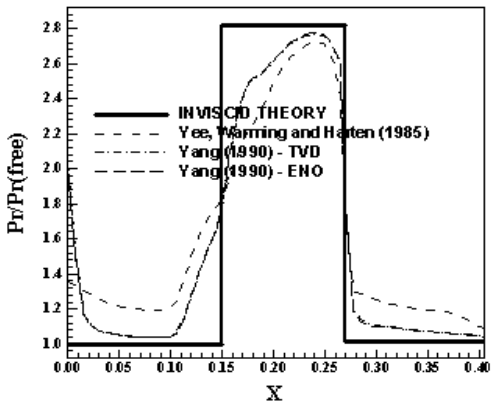

Figure 30. Wall pressure distributions ([15]).

Table 5. Shock angle and respective percentage errors to the ramp problem ([15] case).

Algorithm	β (°)	Error (%)
[6]	53.9	1.70
[14]/TVD	52.8	0.38
[14]/ENO	52.5	0.94

[16] ***Results.*** Figures 31 to 33 exhibit the pressure contours obtained by the [6], the [14]/TVD, and the [14]/ENO schemes, respectively, using the [16] turbulence model. The most severe pressure field, which characterizes the most conservative solution, is again obtained by the [14]/ENO scheme. The shock wave is better captured by the [14] schemes. All schemes detect the weak shock wave formed ahead of the ramp's corner described in the laminar case. With this turbulence model, the extension of the separated flow was similar to the laminar case. Hence, the reduction of the extension of the separated flow is small. Even so, this reduction occurs. However, it results in the [15] model presenting better flow characteristics.

Figures 34 to 36 show the velocity vector fields close to the ramp wall and the respective streamlines obtained by the [6], by the [14]/TVD, and by the [14]/ENO schemes using the [16] turbulence model. It is possible to note regions of separated flow in the solutions generated by all schemes. The streamlines highlight this separated flow close to the wall, as well the formation of a circulation bubble. The separation region detected by the [6] TVD scheme is shorter than the respective ones detected by the [14]/TVD and [14]/ENO schemes. Nonetheless, a thicker boundary layer is characterized in this case.

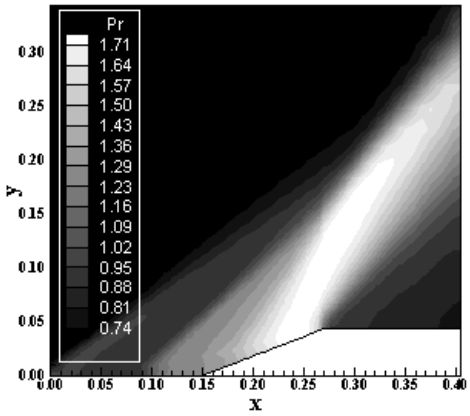

Figure 31. Pressure contours ([6]).

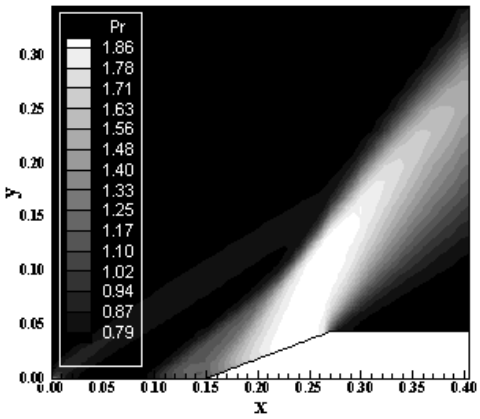

Figure 32. Pressure contours ([14]/TVD).

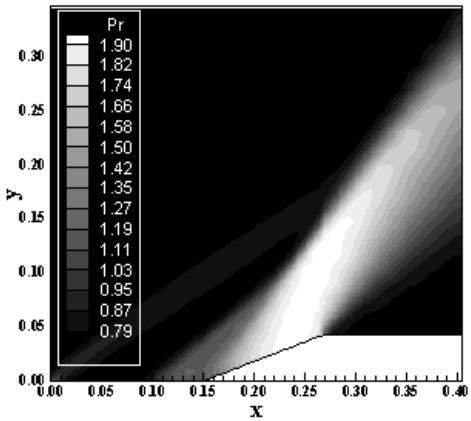

Figure 33. Pressure contours ([14]/ENO).

Figure 37 exhibits the wall pressure distributions obtained by all schemes using the [16] turbulence model. They are compared with inviscid solution. All schemes present a small peak of pressure ahead of the ramp's corner, which defines the weaker shock (approximately at x = 0.130m). Better solutions are obtained by the [14]/TVD and [14]/ENO schemes, with pressure peaks, at the ramp

region, closer to the pressure plateau of the inviscid solution. Both schemes under-predict the pressure plateau. The pressure after the expansion fan is also better captured by the versions of the [14] scheme.

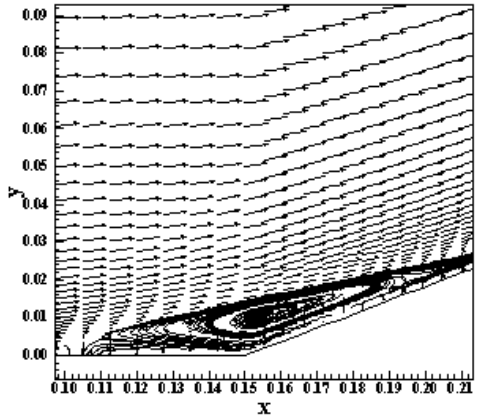

Figure 34. Velocity field and streamlines ([6]).

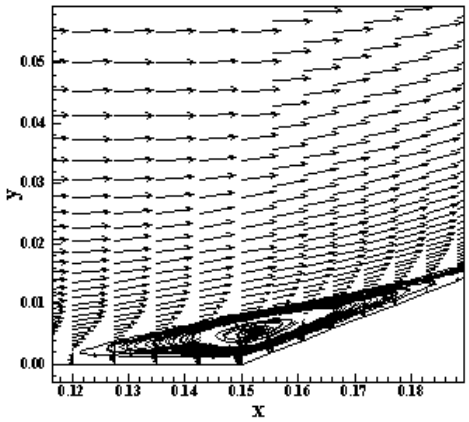

Figure 35. Velocity field and streamlines ([14]/TVD).

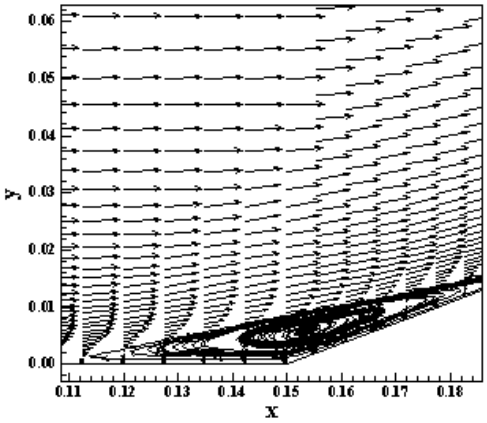

Figure 36. Velocity field and streamlines ([14]/ENO).

Again, it is possible to determine by each scheme the shock angle of the oblique shock wave, β, measured in relation to the initial direction of the flow field. Using a transfer in Figures 31 to 33, it is possible to obtain the values of β to each scheme, as well the respective errors, shown in Tab. 6. As can be observed, all three schemes employing the [16] turbulence model present the same value to the shock angle, with an error of 2.26%.

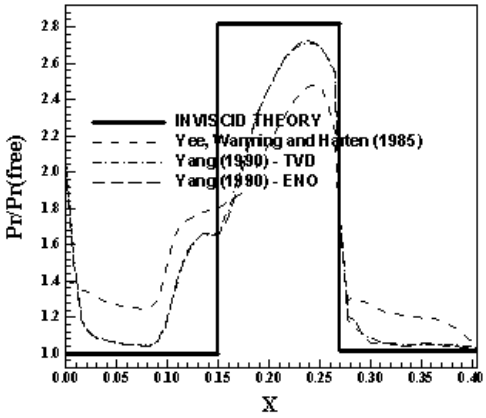

Figure 37. Wall pressure distributions ([16]).

Table 6. Shock angle and respective percentage errors to the ramp problem ([16] case).

Algorithm	β (°)	Error (%)
[6]	51.8	2.26
[14]/TVD	51.8	2.26
[14]/ENO	51.8	2.26

[17] ***Results.*** Figures 38 to 40 exhibit the pressure contours obtained by the [6], the [14]/TVD, and the [14]/ENO schemes, respectively, using the [17] turbulence model. The most severe pressure field, which characterizes the most conservative solution, is again obtained by the [14]/ENO scheme. The shock wave is better captured by the [14] schemes. All schemes detect the weak shock wave formed ahead of the ramp's corner described in the laminar case. With this turbulence model, the extension of the separated flow was similar to the laminar case. Hence, the reduction of the extension of the separated flow is small. Even so, this reduction occurs. However, it results in the [15] model representing better flow characteristics.

Figures 41 to 43 show the velocity vector fields close to the ramp wall and the respective streamlines obtained by the [6], by the [14]/TVD, and by the [14]/ENO schemes using the [17] turbulence model. It is possible to note regions of separated flow in the solutions generated by all schemes. The streamlines highlight this separated flow close to the wall, as well the formation of a circulation bubble. The separation region detected by the [6] TVD scheme is

shorter than the respective ones detected by the [14]/TVD and [14]/ENO schemes. Nonethless, a thicker boundary layer is characterized in this case.

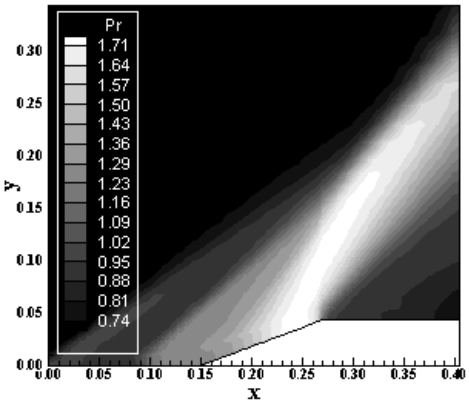

Figure 38. Pressure contours ([6]).

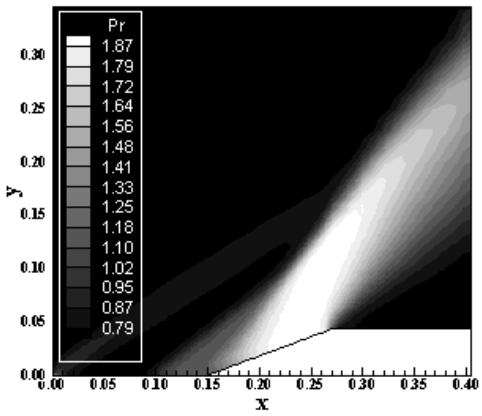

Figure 39. Pressure contours ([14]/TVD).

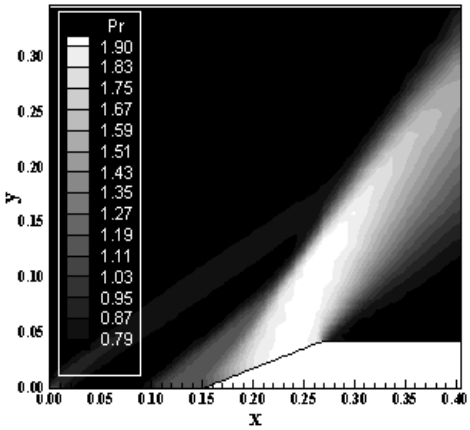

Figure 40. Pressure contours ([14]/ENO).

Figure 44 exhibits the wall pressure distributions obtained by all schemes using the [17] turbulence model. They are compared with inviscid solution. All schemes present a small peak of pressure ahead of the ramp's corner, which defines the weaker shock (approximately at x = 0.130m). Better solutions are obtained by the [14]/TVD and [14]/ENO schemes, with pressure peaks, at the ramp region, closer to the pressure plateau of the inviscid solution. Both schemes under-predict the pressure plateau. The pressure after the expansion fan is also better captured by the versions of the [14] scheme.

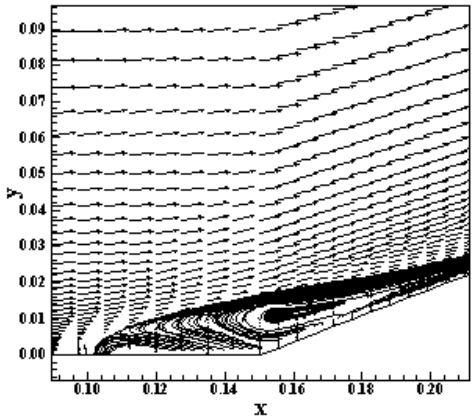

Figure 41. Velocity field and streamlines ([6]).

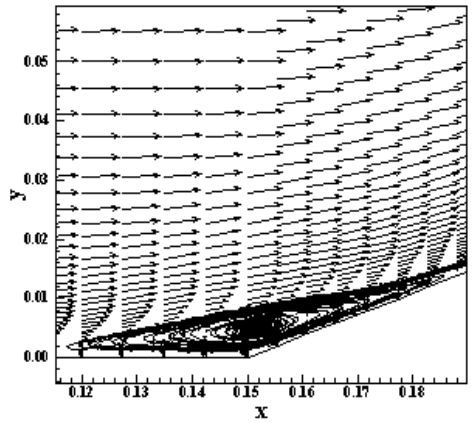

Figure 42. Velocity field and streamlines ([14]/TVD).

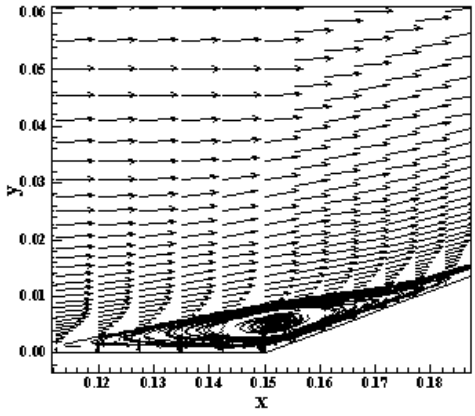

Figure 43. Velocity field and streamlines ([14]/ENO).

Again, it is possible to determine by each scheme the shock angle of the oblique shock wave, β, measured in relation to the initial direction of the

flow field. Using a transfer in Figures 38 to 40, it is possible to obtain the values of β to each scheme, as well the respective errors, shown in Tab. 7. As can be observed, all three schemes employing the [17] turbulence model present the same value to the shock angle, with an error of 2.64%.

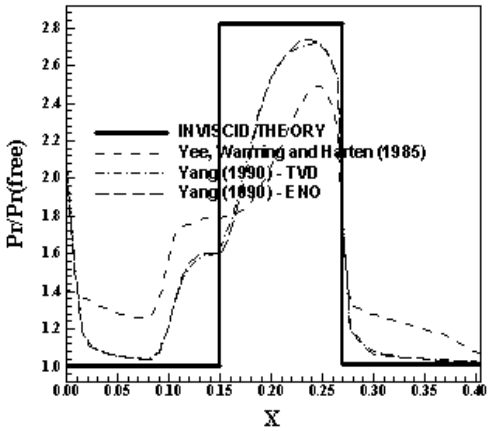

Figure 44. Wall pressure distributions ([17]).

Table 7. Shock angle and respective percentage errors to the ramp problem ([17] case).

Algorithm	β (°)	Error (%)
[6]	51.6	2.64
[14]/TVD	51.6	2.64
[14]/ENO	51.6	2.64

9.3 Computational Costs

Table 8. Computational costs.

Case	Scheme	Cost[(1)]:
Inviscid	[6]	1.061×10^{-4}
	[14]/TVD	1.319×10^{-4}
	[14]/ENO	1.325×10^{-4}
Laminar	[6]	2.260×10^{-5}
	[14]/TVD	2.292×10^{-4}
	[14]/ENO	2.316×10^{-4}
[15] Model	[6]	4.473×10^{-5}
	[14]/TVD	2.733×10^{-4}
	[14]/ENO	2.740×10^{-4}
[16] Model	[6]	2.613×10^{-5}
	[14]/TVD	2.279×10^{-4}
	[14]/ENO	2.295×10^{-4}
[17] Model	[6]	3.107×10^{-5}
	[14]/TVD	2.396×10^{-4}
	[14]/ENO	2.491×10^{-4}

(1): Measured in seconds/per iteration/per cell.

The computational costs of each numerical scheme for the inviscid, laminar and turbulent cases were incorporated in the present work. It gives an idea of the computational complexity of the numerical implementation of each scheme. As can be seen from Table 8, the inviscid-implicit-numerical implementations of each scheme are the cheapest in terms of computational cost. The most expensive implementations are due to the [15] turbulence model. In general terms, the studied schemes present the expected behavior: the [14] versions are more complex than the [6] scheme and it is reflected in their bigger computational costs for each case; the [15] turbulence model requires more quantities to be defined and the [16] turbulence model is more concise, being the [17] model an intermediary between them; and the inviscid simulations are less expensive than the viscous simulations.

10 Conclusions

In the present work, the [6], and the [14] schemes are implemented, on a finite volume context and using a structured spatial discretization, to solve the Euler and the laminar/turbulent Navier-Stokes equations in the two-dimensional space. The [6] scheme and the [14] schemes are TVD or ENO high resolution flux difference splitting ones, based on the concept of Harten's modified flux function. The [6] TVD scheme is second order accurate in space, except at extrema, where the accuracy is reduced to first order. The [14] scheme, in its ENO version, is uniformly second order accurate in space, inclusive at extrema. Its TVD version is also second order accurate in space, except at extrema. An implicit formulation is employed to solve the Euler equations in the inviscid problems. To solve the laminar/turbulent Navier-Stokes equations, an explicit formulation based on a dimensional splitting procedure is employed. Turbulence is taken into account considering two algebraic models, namely: the [15] and the [16] ones, and the one-equation model of [17]. The algorithms are accelerated to the steady state solution using a spatially variable time step, which has demonstrated effective gains in terms of convergence rate ([20-21]). All schemes are applied to the solution of the physical problems of the transonic flow along a convergent-divergent nozzle and the supersonic flow along a compression corner in the inviscid case. To the laminar / turbulent viscous case, the supersonic flow along a ramp is solved. The results have demonstrated that the most severe solutions are obtained with the [6] TVD scheme in the inviscid problems, whereas the [14] algorithm present the most severe solutions in

the viscous problem, in both laminar and turbulent cases. The most accurate results are obtained by the [6] TVD scheme in the nozzle problem, by the [14]/ENO scheme in the corner problem and by the [14]/TVD scheme in the ramp problem, viscous case.

In the inviscid case, it is possible to highlight that the [6] TVD scheme yields the best pressure distribution along the nozzle lower wall. In the compression corner, the [14] schemes present good wall pressure distributions, slightly under-predicting the pressure plateau. The shock transition in all schemes is captured using four cells, which is a good number of cells to high resolution schemes. The shock angle of the oblique shock wave that is formed at the compression corner is best estimated by the [14]/ENO algorithm.

In the ramp viscous case, the laminar results present the [6] and the [14]/ENO schemes as yielding the best values to the shock angle at the ramp. The turbulent results presents the [14]/TVD scheme using the [15] model as presenting the best value to the shock angle at the ramp. The most severe pressure peak at the ramp is due to the [14]/TVD and the [14]/ENO schemes using the [15] turbulence model. All pressure distributions, related to the three algorithms, under-predict the pressure plateau of the inviscid solution - the correct solution considering the boundary layer theory. The most critical pressure distributions, generated by each scheme, are obtained when using the [15] turbulence model. As general conclusion in terms of viscous simulations, all algorithms present the most severe solution considering wall pressure distribution as using the [15] model.

11 Acknowledgments

The present author acknowledges the CNPq by the financial support conceded under the form of a DTI (Industrial Technological Development) scholarship no. 384681/2011-5. He also acknowledges the infra-structure of the ITA that allowed the realization of this work.

References:

[1] R. D. Richtmeyer, and K. W. Morton, *Difference Methods for Initial-Value Problem*, Interscience-Wiley, New York, 1967.

[2] A. Harten, On a Class of High Resolution Total-Variation-Stable Finite-Difference Schemes, *NYU Report*, New York University, New York, October, 1982.

[3] A. Harten, High Resolution Schemes for Hyperbolic Conservation Laws, *Journal of Computational Physics*, Vol. 49, No. 2, 1983, pp. 357-393.

[4] A. Harten, J. M. Hyman, and P. D. Lax, *Commun. Pure Appl. Math*, Vol. 29, 1976, p. 297.

[5] M. G. Crandall, and A. Majda, *Math. Comput.*, Vol. 34, No. 149, 1980, p. 1.

[6] H. C. Yee, R. F. Warming, and A. Harten, Implicit Total Variation Diminishing (TVD) Schemes for Steady-State Calculations, *Journal of Computational Physics*, Vol. 57, No. 3, 1985, pp. 327-360.

[7] A. Harten, and S. Osher, Uniformly High Order Accurate Non-Oscillatory Schemes, *SIAM J. Num. Anal.*, Vol. 24, No. 2, 1987, pp. 279-309.

[8] A. Harten, B. Engquist, S. Osher, and S. R. Chakravarthy, Uniformly High Order Accurate Essentially Non-Oscillatory Schemes. II., *Preprint*, 1986.

[9] A. Harten, B. Engquist, S. Osher, and S. R. Chakravarthy, Some Results on Uniformly High Order Accurate Essentially Non-Oscillatory Schemes, *Advances in Numerical Analysis and Applied Mathematics*, edited by J. C. South, Jr. and M. Y. Hussaini, *ICASE Rept. 86-18*; also *Journal of Applied Num. Mathematics* Vol. 2, 1986, pp. 347-367.

[10] A. Harten, B. Engquist, S. Osher, and S. R. Chakravarthy, Uniformly High Order Accurate Essentially Non-Oscillatory Schemes. III., *ICASE Rept. 86-22*, 1986.

[11] S. K. Godunov, A Finite Difference Method for the Numerical Computation of Discontinuous Solutions of the Equations to Fluid Dynamics, *Mat. Sb.*, Vol. 47, 1958, pp. 271-290.

[12] B. Van Leer, Towards the Ultimate Conservative Difference Scheme. V. A Second Order Sequel to Godunov's Method, *Journal of Computational Physics*, Vol. 32, No. 1, 1979, pp. 101-136.

[13] P. Colella, and P. R. Woodward, The Piecewise-Parabolic Method (PPM) for Gas-Dynamical Simulations, *Journal of Computational Physics*, Vol. 54, No. 1, 1984, pp. 174-201.

[14] J. Y. Yang, Uniformly Second-Order-Accurate Essentially Nonoscillatory Schemes for the Euler Equations, *AIAA Journal*, Vol. 28, No. 12, 1990, pp. 2069-2076.

[15] T. Cebeci, and A. M. O. Smith, A Finite-Difference Method for Calculating Compressible Laminar and Turbulent Boundary Layers, *Journal of Basic Engineering*, Trans. ASME, Series B, Vol. 92, No. 3, 1970, pp. 523-535.

[16] B. D. Baldwin, and H. Lomax, Thin Layer Approximation and Algebraic Model for Separated Turbulent Flows, *AIAA Paper 78-257*, 1978.

[17] P. R. Sparlat, and S. R. Allmaras, A One-Equation Turbulence Model for Aerodynamic Flows, *AIAA Paper 92-0439*, 1992.

[18] Secundov, Smirnova, Kozlov, Gulyaev, One-Equation Eddy Viscosity Model (Modified L. S. J. Kovasznay Model), Short Summary of the Equations, *Personal Communication*, 1990.

[19] Hunt, J. C. R., Turbulence Structure in Thermal Convection and Shear-Free Boundary Layers, *J. Fluid Mech.*, Vol. 138, 1984, pp. 161-184.

[20] E. S. G. Maciel, Analysis of Convergence Acceleration Techniques Used in Unstructured Algorithms in the Solution of Aeronautical Problems – Part I, *Proceedings of the XVIII International Congress of Mechanical Engineering (XVIII COBEM)*, Ouro Preto, MG, Brazil, 2005. [CD-ROM]

[21] E. S. G. Maciel, Analysis of Convergence Acceleration Techniques Used in Unstructured Algorithms in the Solution of Aerospace Problems – Part II, *Proceedings of the XII Brazilian Congress of Thermal Engineering and Sciences (XII ENCIT)*, Belo Horizonte, MG, Brazil., 2008 [CD-ROM]

[22] R. W. Fox, and A. T. McDonald, *Introdução à Mecânica dos Fluidos*, Ed. Guanabara Koogan, Rio de Janeiro, RJ, Brazil, 632p, 1988.

[23] E. S. G. Maciel, Comparison Among Structured High Resolution Algorithms in the Solution of the Euler Equations in Two-Dimensions, *Journal Mecánica Computacional*, Argentina, Vol. XXVI, No. 13, 2007, pp. 1055-1074.

[24] P. L. Roe, Approximate Riemann Solvers, Parameter Vectors, and Difference Schemes, *Journal of Computational Physics*, Vol. 43, No. 2, 1981, pp. 357-372.

[25] E. S. G. Maciel, Comparison Among the First Order Upwind Algorithms of Roe, of Steger and Warming, of Van Leer and of Chakravarthy and Osher in the Solution of the Euler Equations in 2D – Theory, *8th Symposium of Computational Mechanics (VIII SIMMEC)*, Belo Horizonte, MG, Brazil, 2008. [CD-ROM]

[26] L. N. Long, M. M. S. Khan, and H. T. Sharp, Massively Parallel Three-Dimensional Euler / Navier-Stokes Method, *AIAA Journal*, Vol. 29, No. 5, 1991, pp. 657-666.

[27] E. S. G. Maciel, Explicit and Implicit Solutions of First Order Algorithms Applied to the Euler Equations in Two-Dimensions – Part II – Implicit Formulations and Results, *Proceedings of the IX Symposium of Computational Mechanics (IX SIMMEC)*, São João Del Rei, MG, Brazil, 2010. [CD-ROM]

[28] E. S. G. Maciel, Comparação entre os Modelos de Turbulência de Cebeci e Smith e de Baldwin e Lomax, *Proceedings of the 5th Spring School of Transition and Turbulence (V EPTT)*, Rio de Janeiro, RJ, Brazil, 2006.

[29] E. S. G. Maciel, Estudo de Escoamentos Turbulentos Utilizando os Modelos de Cebeci e Smith e de Baldwin e Lomax e Comparação entre os Algoritmos de MacCormack e de Jameson e Mavriplis, *Proceedings of the 7th Symposium of Computational Mechanics (VII SIMMEC)*, Araxá, MG, Brazil, 2006. [CD-ROM].

[30] D. J. Mavriplis, and A. Jameson, Multigrid Solution of the Navier-Stokes Equations on Triangular Meshes, *AIAA Journal*, Vol. 28, No. 8, 1990, pp. 1415-1425.

[31] Maciel, E. S. G., Simulação Numérica de Escoamentos Supersônicos e Hipersônicos Utilizando Técnicas de Dinâmica dos Fluidos Computacional, *Doctoral Thesis*, ITA, São José dos Campos, SP, Brazil, 258p, 2002.

[32] M. L. Mason, L. E. Putnam, and R. J. Re, The Effect of Throat Contouring on Two-Dimensional Converging-Diverging Nozzles at Sonic Conditions, *NASA Technical Paper 1704*, 1980.

[33] J. D. Anderson Jr., *Fundamentals of Aerodynamics*, McGraw-Hill, Inc., EUA, 563p, 1984.